

Unraveling the mysteries of Jets in peculiar NLSy1 galaxies through multi-wavelength variability

Vineet Ojha^{1,★}, Xue-Bing, Wu^{2,1}, Luis C. Ho^{1,2}, Raj Prince³, Joysankar Majumdar⁴, Hum Chand⁵, and Chi-Zhuo Wang^{2,1}

¹ Kavli Institute for Astronomy and Astrophysics, Peking University, Beijing 100871, China

² Department of Astronomy, School of Physics, Peking University, Beijing 100871, China

³ Department of Physics, Institute of Science, Banaras Hindu University, Varanasi, 221005, Uttar Pradesh, India

⁴ Astronomical Observatory, University of Warsaw, Al. Ujazdowskie 4, 00-478, Warsaw, Poland

⁵ Department of Physics and Astronomical Science, Central University of Himachal Pradesh, Dharamshala, 176215, India

Received February 30, 20XX

ABSTRACT

Context. Radio-quiet narrow-line Seyfert 1 galaxies (RQ-NLSy1s) are generally considered to be dominated by thermal emission from the accretion disk. However, detections of recurring flaring at 37 GHz by the Metsähovi Radio Observatory from seven RQ-NLSy1s suggest that non-thermal processes may also contribute to their observed emission.

Aims. We perform a systematic optical and mid-infrared (MIR) variability study along with broadband SED modeling of them to investigate the origin of their flux variations and assess the relative contributions of the accretion disk and potential jet-related components.

Methods. High-cadence optical light curves in the g , r , and i bands were obtained from the *Zwicky Transient Facility (ZTF)*, and long-term MIR light curves in the $W1$ and $W2$ bands from the *Wide-field Infrared Survey Explorer*. Optical variability was quantified using the F_{AGN} -test, the peak-to-peak variability amplitude (ψ_{pp}), and fractional variability (F_{var}), while MIR variability was characterized by the redshift-corrected intrinsic variability amplitude. Optical variability was examined on timescales from intra-night to long-term, and MIR variability on long-term timescales. Color-magnitude behavior was analyzed using bias-resistant representations, and correlations with the physical parameters of AGN were explored.

Results. All seven sources exhibit statistically significant long-term optical variability, with variability amplitudes systematically increasing toward shorter wavelengths across the investigated timescales. In three sources, exhibiting pronounced bluer-when-brighter trends, both ψ_{pp} and F_{var} increase across the *ZTF* bands, indicative of a non-thermal contribution. Intrinsic MIR variability is detected in three of the four sources. Significant optical-MIR and MIR intra-band lags are observed, while intra-band optical lags are not statistically significant in the sample. Optical variability amplitudes are anti-correlated with the Eddington ratio and emission-line ratios and positively correlated with black hole mass.

Conclusions. A subset of RQ-NLSy1s exhibits variability patterns similar to jet-dominated AGNs, suggesting that weak or intermittent jets are contributing to their optical and MIR emission. Broadband SED modeling of these sources further supports this scenario. Coordinated multi-wavelength monitoring is needed to further constrain the physical origin of these variations.

Key words. surveys – galaxies: active – galaxies: jets – γ -ray-galaxies: photometry – galaxies: Seyfert – radio continuum: galaxies

1. Introduction

Active galactic nuclei (AGNs) are among the most luminous and variable objects in the Universe, powered by accretion onto supermassive black holes with masses of $\sim 10^6$ – $10^{10} M_{\odot}$ (Lynden-Bell 1969; Rees 1984; Woo & Urry 2002; Bischetti et al. 2017). Variability observed across the electromagnetic spectrum, on timescales ranging from minutes to decades, provides a powerful probe of the physical processes operating in the immediate vicinity of the black hole, including accretion dynamics and relativistic outflows (Urry & Padovani 1995; Ulrich et al. 1997; Czerny et al. 2008). However, the origin of observed optical variability remains debated, as classical disk models predict characteristic timescales that are often longer than those inferred from observations (Czerny et al. 2008; MacLeod et al. 2010). This has motivated alternative interpre-

tations involving disk instabilities, localized temperature fluctuations, reprocessing of high-energy emission, or additional non-thermal contributions from relativistic jets (Kawaguchi et al. 1998; Lawrence 2018; Noda & Done 2018). Although only a small fraction of AGNs are known to host powerful relativistic jets, traditionally identified through strong radio emission (Kellermann et al. 1989; Urry & Padovani 1995), the jet power and radiative output are expected to scale non-linearly with black hole mass. As a result, jet signatures in low-mass, rapidly accreting AGNs may be intrinsically weak at radio frequencies, rendering radio loudness an incomplete tracer of jet activity in such systems, particularly in radio-quiet sources with narrow emission lines and high Eddington ratios (Heinz & Sunyaev 2003; Foschini 2014; Caccianiga et al. 2015; Jarvela et al. 2017; Padovani 2017).

Narrow-line Seyfert 1 (NLSy1) galaxies represent one such particular subclass of AGN. These are traditionally defined by narrow permitted emission lines with $\text{FWHM}(\text{H}\beta) < 2000 \text{ km}$

* Corresponding author: vineetojhabhu@gmail.com, wuxb@pku.edu.cn

s^{-1} , weak [O III] emission relative to H β , and often strong Fe II multiplets (Osterbrock & Pogge 1985; Goodrich et al. 1989; Véron-Cetty et al. 2001). NLSy1s typically host relatively low-mass black holes, accreting at high Eddington ratios, and are often considered to represent an early phase of AGN evolution (Mathur 2000; Grupe & Mathur 2004; Zhou et al. 2006; Komossa 2018; Paliya 2019; Ojha et al. 2020). Although the majority of NLSy1s are radio-quiet, the discovery of radio-loud and especially γ -ray-detected NLSy1s (γ -NLSy1s) has demonstrated that relativistic jets can be launched even in systems with comparatively lower black hole masses and high accretion rates (Abdo et al. 2009a,b,c; Foschini 2011; Foschini et al. 2015; Ojha 2022). The presence of relativistic jets in NLSy1s has profound implications for our understanding of jet formation in low luminous AGNs, as these sources occupy a region of parameter space traditionally thought to be unfavorable for jet launching (Mathur 2000; Foschini 2011, 2017). Unlike BL Lac objects, where low jet power is often attributed to radiatively inefficient accretion (Heckman & Best 2014), NLSy1s exhibit radiatively efficient accretion flows and systematically high Eddington ratios (Brandt et al. 1997; Grupe & Mathur 2004; Zhou et al. 2006; Ojha et al. 2020). Their jet properties therefore challenge earlier paradigms and suggest that jet production is not suppressed at high accretion rates (Foschini et al. 2015; Padovani 2017). Recent numerical simulations further support this view, suggesting that powerful, collimated jets can form even at near- or super-Eddington accretion rates under suitable magnetic conditions (McKinney et al. 2017; Liska et al. 2022). These developments imply that previous observational biases, particularly the emphasis on radio-loud systems, may have obscured a broader diversity of jet phenomena in AGNs (Berton et al. 2017; Padovani 2017).

In this context, time-domain investigations provide a particularly sensitive means of probing the presence and influence of relativistic jets, especially when traditional radio-based diagnostics become ambiguous and link rapid optical fluctuations with jet activity in AGNs (Wagner & Witzel 1995; Ulrich et al. 1997; Gopal-Krishna et al. 2003; Ojha et al. 2024). Strong and frequent intra-night optical variability (INOV) is commonly observed in jet-dominated sources such as blazars and high-polarization quasars, with duty cycles exceeding 30% (Jang & Miller 1995; de Diego et al. 1998; Stalin & Srianand 2005; Goyal et al. 2012). In contrast, radio-quiet quasars generally show weaker and less frequent INOV, consistent with variability driven by accretion-disk processes or weak, misaligned jets (Chakrabarti & Wiita 1993; Mangalam & Wiita 1993; Goyal et al. 2013a). Among NLSy1s, γ -ray-detected and radio-loud sources display blazar-like INOV characteristics, suggesting the connection between rapid optical variability and relativistic jet emission (Paliya et al. 2013; Ojha et al. 2022, 2024; Singh et al. 2025).

Moreover, color variability behavior of AGNs provides a powerful diagnostic of dominant emission processes, since color-magnitude trends encode the relative contributions of thermal accretion-disk emission and non-thermal synchrotron radiation from relativistic jets, with the direction and strength of the trend depending on the source type and underlying physical conditions (Vagnetti et al. 2003; Gu & Ai 2011; Negi et al. 2022; Ojha et al. 2024). For instance, in jet-dominated AGNs such as BL Lac objects, optical color variability is frequently characterized by a bluer-when-brighter (BWB) trend, commonly attributed to changes in synchrotron emission from the relativistic jet (e.g., Villata et al. 2002; Ikejiri et al. 2011). Within the shock-in-jet framework, freshly accelerated high-energy elec-

trons at the shock front preferentially enhance short-wavelength emission and on shorter timescales than long-wavelength emission, resulting in larger variability amplitudes at higher frequencies (see Kirk et al. 1998; Mastichiadis & Kirk 2002; Türler 2011). Alternative mechanisms, such as energy injection through internal shocks and variations in the Doppler beaming factor, can also naturally cause BWB behavior (e.g., Villata et al. 2004; Papadakis et al. 2007; Larionov et al. 2010).

A major challenge to this framework has emerged with the discovery of seven radio-quiet (or radio-silent) NLSy1 galaxies exhibiting recurrent, high-amplitude flaring at 37 GHz (Lähteenmäki et al. 2018). These sources show dramatic radio variability on timescales of days, reaching flux densities typically associated with powerful jetted AGNs. However, follow-up interferometric observations at lower radio frequencies with the Karl G. Jansky Very Large Array and the Very Long Baseline Array have revealed either very steep radio spectra or non-detections, with no evidence for persistent large-scale relativistic jets (Berton et al. 2020; Jarvela et al. 2024). Several physical explanations have been proposed, including compact and self-absorbed jets, strong free-free absorption by dense ionized gas, jet-interstellar medium interactions, or transient energy-release processes such as magnetic reconnection near the black hole (Antonucci & Barvainis 1988; Bicknell et al. 1997; Jarvela et al. 2024). Apart from constraints from radio studies, the intra-night optical variability detected in a subset of the sources in this sample has been suggested to originate not only from relativistic jets but also from magnetic reconnection events in the black hole magnetosphere (see Ojha et al. 2024). Regardless of the interpretation, these objects challenge the traditional radio-based classification of AGNs and raise questions about the reliability of radio loudness as a diagnostic for jets. Furthermore, optical spectroscopic studies have shown that, despite their extraordinary radio behavior, the emission-line properties of these seven sources are largely consistent with those of typical NLSy1s. They generally exhibit strong Fe II emission and black hole masses that are not exceptional within the class, suggesting that their extreme radio variability is not simply driven by usual accretion-related properties (Crepaldi et al. 2025). This apparent disparity between radio variability and optical spectral properties emphasizes the importance of time-domain and multi-wavelength diagnostics.

In this context, optical and infrared variability studies provide a crucial and complementary probe of the physical components of AGNs. Optical variability primarily traces emission from the accretion disk, with a possible contribution from any jet component extending to these wavelengths, whereas mid-infrared (MIR) emission is generally associated with thermal radiation from dust in the circumnuclear torus (Antonucci 1993; Urry & Padovani 1995). Dust reverberation mapping studies have shown that MIR variability commonly lags optical variations, thereby providing direct constraints on the size, geometry, and structure of the dusty region (Suganuma et al. 2006; Koshida et al. 2014; Mandal et al. 2018). Moreover, the presence or absence of optical intra-band and optical-MIR inter-band time lags serves as a powerful diagnostic of the dominant variability mechanism. For instance, significant lags are expected when variability is disk-dominated and driven by reprocessing (e.g., Cackett et al. 2007; McHardy et al. 2014), whereas jet-dominated variability is expected to exhibit weak or negligible lags owing to its compact and non-thermal origin (e.g., Villata et al. 2002; Marscher et al. 2008).

Despite the availability of high-cadence optical and infrared data from modern time-domain surveys such as the Zwicky

Transient Facility (*ZTF*, Bellm et al. 2019) and the Wide-field Infrared Survey Explorer (*WISE*, Wright et al. 2010), detailed multi-wavelength variability studies of radio-quiet NLSy1 galaxies remain scarce. This is particularly true for sources that exhibit indirect yet compelling evidence for relativistic jet activity. The seven radio-quiet NLSy1s displaying extreme flaring at 37 GHz therefore occupy a uniquely informative parameter space, as they blur the traditional distinction between radio-quiet and jetted AGNs, challenge standard unification schemes, and provide a rare opportunity to investigate the interplay between accretion processes, jet activity, and circumnuclear structures in low- to intermediate-mass black hole systems. In addition, broadband spectral energy distribution (SED) modeling of these RQ-NLSy1s enables an assessment of the relative contributions of thermal emission from the accretion disk and dusty torus versus non-thermal, jet-related components, thereby offering an independent and complementary consistency check on the physical interpretation inferred from variability diagnostics, along with robust constraints on key SED parameters. Motivated by the above considerations, we undertake a comprehensive optical and mid-infrared variability study of seven RQ-NLSy1s that exhibit extreme and recurring 37 GHz radio flaring. By combining analyses of optical variability on timescales from hours to years, long-term mid-infrared variability, optical and mid-infrared color variability, optical–infrared time-lag measurements, and broadband SED modeling, we aim to probe the relative contributions of accretion-driven and jet-related processes in these sources. We also examine how the variability amplitudes of these RQ-NLSy1s relate to their fundamental AGN properties, aiming to identify which physical parameters most strongly influence their variability amplitude. This article is organized as follows. Section 2 outlines the compilation of the data sets used in this study. The analysis techniques and methodological framework are presented in Sect. 3. Our results of the present work are reported in Sect. 4. Discussions are interpreted in Sect. 5, while the main conclusions are summarized in Sect. 6.

2. Data compilation

2.1. ZTF *g*, *r*, and *i* bands optical photometric data

Optical photometric light curves for the seven RQ-NLSy1s were obtained from *ZTF* in the *g*, *r*, and *i* bands using the 23rd public data release (see Masci et al. 2019). Data were retrieved via the NASA/IPAC Infrared Science Archive (IRSA¹) application programming interface within an arcsec radius of the optical source positions. The availability of *ZTF* data for individual sources in the different bands of *ZTF* *g*, *r*, and *i*, together with their basic properties, is reported in Table 1.

To minimize artificial variability introduced by independent photometric calibrations across different *ZTF* fields and CCD quadrants, we retained, for each source and filter, only the light curve corresponding to the observation ID containing the maximum number of data points. The standard quality cuts were then applied following the recommendations of the *ZTF* Science Data System². Specifically, only measurements with catflags = 0 were selected, photometric points with magnitude uncertainties greater than 10% were excluded, and a global 3 σ clipping was applied to remove outliers. In addition, a minimum of five valid data points per band was imposed. This has resulted in *ZTF* *g*-, *r*-, and *i*-band data for all except the *i*-band data for RQ-NLSy1

J102906.69+555625.2 (see Table 1). The resulting light curves are characterized by cadences as short as approximately less than a day (hour-like timescale) and maximum temporal baselines of up to \sim 2200 days, depending on the source and bands. These data are suitable for probing lower optical variability in the current sample of RQ-NLSy1s across both short and long timescales. A representative example of long-term light curves in the *ZTF r* band for these seven RQ-NLSy1s is presented in Fig. 1.

2.2. WISE *W1* and *W2* bands mid-infrared data

The mid-infrared photometric data for the seven RQ-NLSy1s were retrieved from the *WISE* Multiepoch Photometry (MEP) database and the *NEOWISE-R* single-exposure (L1b) source catalog via IRSA³. The combined data set spans the period from 2010 to 2024, with a gap between 2011 and 2014 associated with the cryogen depletion phase of the original *WISE* mission. The availability of *WISE* data for each source in *WISE W1* and *W2* bands is summarized in Table 1. Our analysis was restricted to the *W1* and *W2* bands, as the *W3* and *W4* bands are sparsely sampled and largely confined to the early mission phase. To ensure robust photometry, we applied strict selection criteria to the single-exposure measurements. We selected reduced χ^2 values of profile-fit photometry to be less than 5 in both bands, fewer than three PSF components in the fit, the highest image quality flag, the absence of known artifacts, and no active deblending. In addition, a minimum of five valid data points per band was imposed, and a global 3 σ clipping was also used to remove outliers. This has resulted in a sample of four RQ-NLSy1s with reliable measurements in *WISE W1* and *W2* bands (see Table 1)

Inspection of the resulting light curves revealed closely spaced measurements separated by approximately 11 seconds during individual *WISE* visits. Given the *WISE* orbital period of about 1.5 hours, such measurements were averaged within each visit to construct the final *W1* and *W2* light curves. The processed mid-infrared data provide long-term temporal coverage suitable for investigating MIR variability in RQ-NLSy1s and for comparison with variability observed at other wavelengths. We have shown long-term MIR light curves for the available targets RQ-NLSy1-J122844.81+501751.2, RQ-NLSy1-J123220.11+495721.8, RQ-NLSy1-J150916.18+613716.7, and RQ-NLSy1-J164100.10+345452.7 in the *WISE W1* and *W2* bands of the current sample in Fig. 2.

2.3. Compilation of multi-wavelength data for SED fitting

For the SED fitting of the seven RQ-NLSy1s, we compiled data from the NASA/IPAC Extragalactic Database⁴. Furthermore, we have added available X-ray data from the *SWIFT* and gamma-ray data from the *Fermi-LAT*. However, the latest radio data for all these RQ-NLSy1s were taken from Table 3 of Jarvela et al. (2024). While the literature search reveals that some of the objects had been detected in gamma-ray and in some cases, an upper limit can be estimated to constrain the broadband SED. The initial check on the broadband SED suggests a similar double-hump structure as seen in jet-dominated objects such as blazars. Since these objects have not been monitored in the past for the purpose of SED modeling, the data suffer from non-simultaneity. However, here our objective is not to derive the best fit parameters for the model but rather to qualitatively discuss if these

¹ <https://www.ztf.caltech.edu/ztf-public-releases.html>

² https://irsa.ipac.caltech.edu/data/ZTF/docs/ztf_explanatory_supplement.pdf

³ <https://irsa.ipac.caltech.edu/Missions/wise.html>

⁴ <https://ned.ipac.caltech.edu/>

sources could have possible jet and non-thermal emission as seen in a jetted object.

3. Methodology for analysis

Before performing the variability analysis, all observed *ZTF* light curves were corrected for foreground Galactic extinction and absorption. For each source, the extinction value (A_V) was obtained from the NASA/IPAC Extragalactic Database (NED), and the correction was applied following the prescription of Schlafly & Finkbeiner (2011). Examples of extinction-corrected *ZTF* *r*-band light curves for the seven RQ-NLSy1s are presented in Fig. 1.

3.1. Variability analysis in Optical wavelength

The optical variability properties of the seven RQ-NLSy1s were examined using their *ZTF* *g*, *r*, and *i* band light curves. To assess whether the observed fluctuations are statistically significant, we applied the *F*-test, which is widely adopted in AGN variability studies (Goyal et al. 2012). The robustness and applicability of this approach for NLSy1s have been demonstrated in our previous work (see, Ojha et al. 2018, 2024).

The variability statistic is defined as

$$F_{\text{AGN}} = \frac{s_{\text{lc}}^2}{\kappa^2 \bar{\epsilon}^2} \quad (1)$$

where s_{lc}^2 represents the variance of the observed light curve, and

$$\bar{\epsilon}^2 = \frac{1}{N} \sum_{i=1}^N \epsilon_i^2$$

is the mean squared formal photometric uncertainty for the N^{th} data points. The factor κ accounts for the systematic underestimation of photometric errors.

Reliable characterization of measurement uncertainties is essential for robust variability analyses, particularly when source magnitudes are derived using aperture photometry. It is well established that commonly used aperture-based photometric reduction packages, including IRAF⁵ and DAOPHOT II⁶, tend to underestimate formal magnitude errors, typically by factors of about 1.3–1.75 (Sagar et al. 2004; Bachev et al. 2005). To account for this systematic effect, Goyal et al. (2013b) introduced a correction factor of $\kappa = 1.54$, derived from an extensive set of intra-night AGN monitoring observations.

In contrast, the *ZTF* photometric pipeline determines source magnitudes using a point-spread-function fitting at the target position (Masci et al. 2019; Dekany et al. 2020). As a result, the associated rms photometric uncertainties are not expected to suffer from the same level of underestimation characteristic of aperture-based reductions. Therefore, in this work, we adopted $\kappa = 1$ for the *ZTF* light curves, consistent with the approach followed in recent variability studies based on *ZTF* data (e.g., see Negi et al. 2023; Chand & Gopal-Krishna 2024).

Thus, for each light curve, the computed value of F_{AGN} was compared with the critical value of the *F*-distribution at a significance level of $\alpha = 0.01$, corresponding to a confidence level of 99% for a variability detection. A source was shortlisted as optically variable when F_{AGN} exceeded the critical threshold, thus

rejecting the null hypothesis of non-variability with high confidence.

To characterize the amplitude of the detected optical variability and intrinsic fractional variability, we estimated two complementary quantities: the peak-to-peak variability amplitude and the fractional variability amplitude.

The peak-to-peak amplitude is defined as (Heidt & Wagner 1996)

$$\psi_{\text{pp}} = \sqrt{(m_{\text{max}} - m_{\text{min}})^2 - 2\sigma_{\text{corr}}^2} \quad (2)$$

where m_{max} and m_{min} are the maximum and minimum magnitudes in the light curve, respectively, and

$$\sigma_{\text{corr}}^2 = \kappa^2 \bar{\epsilon}^2$$

is the mean rms error for the data points in the light curve.

The intrinsic fractional variability, which quantifies the source variability after removing the contribution of measurement noise, was calculated following Vaughan et al. (2003) as

$$F_{\text{var}} = \sqrt{\frac{s_{\text{obs}}^2 - \bar{\epsilon}^2}{\langle f \rangle^2}}, \quad (3)$$

where s_{obs}^2 is the sample variance of the flux measurements and $\langle f \rangle$ is the mean flux. The uncertainty associated with F_{var} was calculated using the prescription given by Vaughan et al. (2003). For each of the seven RQ-NLSy1s, we list the full temporal baseline of the *ZTF* light curves, the number of data points in each light curve, and all optical variability diagnostics (F_{AGN} , variability status, ψ_{pp} , and F_{var}) in Table 2. The quoted duration refers to the total observed time span of the light curves. However, Table 3 summarizes, for each source, the number of variable epochs and the total number of available epochs on intranight, week-like, month-like, and year-like timescales. In Fig. 3, a representative set of light curves is presented for intranight, week-like, and month-like timescales for each RQ-NLSy1s, showing their variability nature on different timescales.

3.1.1. Duty cycle of variability

Since AGN variability is not continuous in time, we quantified its occurrence using the duty cycle (DC), which measures the fraction of time during which a source exhibits statistically significant variability. The DC was calculated following the formalism introduced by Romero et al. (1999) and subsequently applied by Staln et al. (2004).

The duty cycle is expressed as

$$\text{DC} = 100 \frac{\sum_{j=1}^M V_j (\Delta t_j)^{-1}}{\sum_{j=1}^M (\Delta t_j)^{-1}} \quad (4)$$

where $\Delta t_j = \Delta t_{\text{obs}, j} / (1 + z)$ is the rest-frame duration of the j^{th} monitoring interval. The indicator V_j is set to unity when variability is detected and zero otherwise.

The resulting DC values, together with the mean values of ψ_{pp} ($\bar{\psi}_{\text{pp}}$) in the *g*, *r*, and *i* bands for each RQ-NLSy1 galaxy for the investigated timescales, are tabulated in Table 4. Note that only light curves classified as variable were included in the calculation of $\bar{\psi}_{\text{pp}}$.

⁵ <http://iraf.noao.edu/>

⁶ <http://www.astro.wisc.edu/sirtf/daophot2.pdf>

Table 1: Summary of multiwavelength data coverage and basic source properties of the seven radio-quiet narrow-line Seyfert 1 galaxies, including redshift, R-band magnitude, radio-loudness parameter, and black hole mass.

SDSS Name ^a	RA.	DEC.	z ^b	m _R ^c	RL ^d	M _{BH} ^e (M _⊙)	ZTF-data			WISE-data		SWIFT-data	
							g	r	i	W1	W2	X-ray	
J102906.69+555625.2	157.27788	55.94033	0.451	19.1	—	10 ^{7.33}	✓	✓	✗	✗	✗	✓	
J122844.81+501751.2	187.18671	50.29756	0.262	17.8	2.4	10 ^{6.84}	✓	✓	✓	✓	✓	✓	
J123220.11+495721.8	188.08379	49.95606	0.262	16.9	0.1	10 ^{7.30}	✓	✓	✓	✓	✓	✓	
J150916.18+613716.7	227.31742	61.62131	0.201	18.6	—	10 ^{6.66}	✓	✓	✓	✓	✓	✓	
J151020.06+554722.0	227.58358	55.78944	0.150	17.8	0.5	10 ^{6.67}	✓	✓	✓	✗	✗	✓	
J152205.41+393441.3	230.52254	39.57814	0.077	13.1	1.7	10 ^{5.97}	✓	✓	✓	✗	✗	✓	
J164100.10+345452.7	250.25042	34.91464	0.164	16.0	0.8	10 ^{7.15}	✓	✓	✓	✓	✓	✓	

^a The SDSS names of the source.

^b Redshift of the sources are taken from Lähteenmäki et al. (2018).

^c The apparent R-band magnitude of the sources are taken from Monet (1998).

^d Radio-loudness parameter $RL \equiv F_{5.2\text{ GHz}}/F_{B\text{-band}}$ of current sources are taken from Crepaldi et al. (2025)

^e Black hole masses of current sources are taken Lähteenmäki et al. (2018).

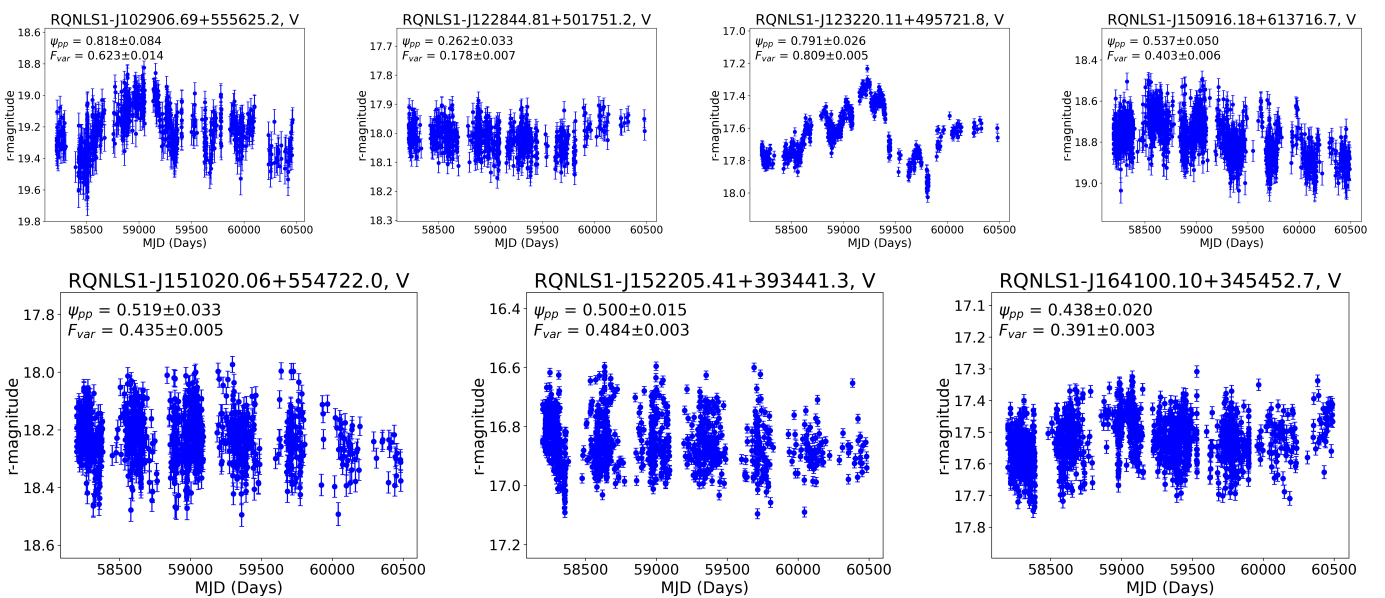


Fig. 1: Long-term r-band ZTF light curves of the seven RQ-NLSy1s from the current sample, showing variability (V) from all the sources on a year-like timescale. The name and long-term variability status of each RQ-NLSy1 galaxy are presented in the title of each panel, and estimated variability parameters ψ_{pp} and F_{var} are displayed in the upper-left corner of each panel.

3.2. Variability analysis in mid-infrared wavelength

The mid-infrared variability of the seven RQ-NLSy1s was quantified using the intrinsic variability amplitude, a metric commonly employed in MIR variability studies (e.g. Rakshit et al. 2019; Anjum et al. 2020; Wang & Shi 2020). This approach measures the scatter in the observed magnitudes after accounting for the measurement uncertainties (Sesar et al. 2007; Ai et al. 2010). We adopt this estimator for the MIR analysis because *WISE* light curves are generally sparsely sampled and are affected by larger photometric and systematic uncertainties compared to optical data, which limits the robustness of multi-parameter variability estimators commonly applied at optical wavelengths. The adopted formalism explicitly accounts for measurement errors and incorporates systematic uncertainties associated with the *WISE* W1 and W2 bands, as characterized by Jarrett et al. (2011) for the mission (Wright et al. 2010). This

approach has been widely used to reliably quantify intrinsic MIR variability in AGN and related sources (e.g. Sesar et al. 2007; Ai et al. 2010; Rakshit et al. 2019). Therefore, the use of this estimator ensures a homogeneous and robust assessment of MIR variability and facilitates a direct comparison with previous studies.

The observed dispersion of the MIR light curve is given by

$$\sigma_{\text{MIR}} = \sqrt{\frac{1}{N-1} \sum_{i=1}^N (m_i - \langle m \rangle)^2} \quad (5)$$

where m_i denotes the magnitude at i^{th} epoch and $\langle m \rangle$ is the weighted mean magnitude.

The intrinsic variability amplitude is then defined as

$$V_{\text{int}} = \begin{cases} \sqrt{\sigma_{\text{MIR}}^2 - \sigma_{\text{err}}^2}, & \sigma_{\text{MIR}} > \sigma_{\text{err}} \\ 0, & \text{otherwise} \end{cases} \quad (6)$$

where

$$\sigma_{\text{err}}^2 = \frac{1}{N} \sum_{i=1}^N \delta_i^2 + \delta_{\text{sys}}^2$$

combines individual photometric uncertainties δ_i with systematic errors δ_{sys} , adopted to 0.024 mag for *W1* and 0.028 mag for *W2* (Jarrett et al. 2011).

Assuming independent and normally distributed measurements, the uncertainty in σ_{MIR} can be approximated to $\sigma_{\text{MIR}}/\sqrt{2(N-1)}$ (e.g., see Ojha et al. 2025). To correct for the redshift of the object, we computed the rest-frame V_{mz} by multiplying V_{int} with $\sqrt{1+z}$ following Rakshit et al. (2019)

$$V_{\text{mz}} = V_{\text{int}} \sqrt{1+z}. \quad (7)$$

A source was considered variable in the MIR if $V_{\text{mz}} \gtrsim 0.1$. The MIR variability amplitudes of the rest-frame and their uncertainties for individual sources in *WISE W1* and *W2* are tabulated in Table 2.

3.3. Color behavior

The optical radiation detected from AGNs is generally understood as a superposition of two physically distinct components: quasi-thermal emission associated with the accretion disk and non-thermal synchrotron emission produced by relativistic jets. Investigating color variability, therefore, provides a useful diagnostic in probing the dominant contributions between these components to the observed flux. In a similar context, infrared emission, which primarily traces optical and ultraviolet radiation re-processed by circumnuclear dust, offers complementary insight into the coupling between thermal and non-thermal processes in AGNs (see, e.g., Storchi-Bergmann et al. 1992; Lu et al. 2016). Since AGNs can exhibit variability on hour-like time scales, this can bias color measurements if non-simultaneous data are combined. To ensure a reliable characterization of spectral variations, we therefore required observations in different bands to be quasi-simultaneous. Following the criterion adopted by Ojha et al. (2025), only data points obtained within a 30-minute interval in the relevant bands were used for the color analysis, thus minimizing the influence of intrinsic flux variability on the derived colors. In addition, we required at least five quasi-simultaneous measurements per source to ensure statistical robustness. The same selection criteria were consistently applied to the mid-infrared data. Consequently, the optical and MIR color variability analysis presented here is based on a subset of available light-curve data, restricted to observations that satisfy these temporal and sampling constraints.

For the seven RQ-NLSy1s that meet the above criterion, we constructed color-magnitude diagrams using quasi-simultaneous data in the optical and MIR bands. Specifically, we examine the relations $g-r$ versus r , $r-i$ versus i , and $W1-W2$ versus $W2$. In these diagrams, the magnitude at the longer wavelength was initially placed along the abscissa, whereas the color index, defined as the difference between the shorter and longer wavelength magnitudes, was plotted on the ordinate. This choice ensures a uniform approach across the optical and MIR wavelengths. However, during the analysis, we found that the inferred color-magnitude trend can reverse when the shorter-wavelength (bluer) magnitude is used on the abscissa, an effect that is particularly noticeable in the color-magnitude diagrams $g-r$ versus r and $g-r$ versus g (see Fig. 4). To account for this behavior and to

test the robustness of the trends, we therefore constructed three alternative representations for each source: $(m_1 - m_2)$ versus m_2 , $(m_1 - m_2)$ versus m_1 , and $(m_1 - m_2)$ versus $(m_1 + m_2)$. Representative examples of these long-term color-magnitude relations in optical and MIR wavelengths are shown in Figs. 4, 5, 6. For each diagram, the dependence between color and magnitude was quantified using orthogonal distance regression, which accounts for uncertainties in both variables. In addition, the Pearson correlation coefficient, ρ_r , was calculated to characterize the strength and direction of the correlation.

To assess the presence of systematic color trends, we classified sources based on the value of the Pearson rank correlation coefficient (ρ_r). A positive correlation with $\rho_r \geq 0.5$ was interpreted as a BWB trend, while a negative correlation with $\rho_r \leq -0.5$ was taken to indicate a redder-when-brighter (RWB) trend. Sources with intermediate values of $-0.5 < \rho_r < 0.5$ were considered to show no statistically significant color-magnitude correlation (denoted as NOT). All color-magnitude representations from optical to MIR are presented in Figs. 4, 5, 6, and in the left corner of each sub-panel, the best-fit slope and ρ_r (Pearson- ρ) values are shown for each source.

3.4. Lag Measurement

The multi-wavelength light curves exhibit pronounced variability and a high degree of coherence, with recurring features such as maxima and minima appearing at the corresponding epochs. This strong correlation enables a reliable estimation of intra-band and inter-band time delays. We therefore computed the intra-band and inter-band lags using the interpolated cross-correlation function (ICCF) in conjunction with flux randomization and random subset sampling (FR/RSS), following the implementation of Peterson et al. (2004). For optical intera-band lag measurements, the *ZTF* light curves were binned using a 1-day window and subsequently used for the ICCF and FR/RSS analysis. For optical-infrared lag measurements, we adopted a 180-day binning window for the *WISE* light curves and a 10-day binning window for the *ZTF* light curves. All optical intera-band lags were measured with respect to the g band, as it lies closest to the thermal emission peak of the accretion disk among the g , r , and i bands. The time lag was derived from the centroid of the cross-correlation function (CCF), considering only correlation coefficients that exceeded 80% of the peak value. Uncertainties on the lag measurements were quantified using the FR/RSS method. For each band pair, 1000 FR/RSS realizations were generated by randomly resampling the light curves with replacement and perturbing the fluxes according to their measurement uncertainties. The centroid lag was measured for each realization, yielding a centroid cross-correlation distribution (CCCD). The final lag was taken as the median of the CCCD, with the 1σ uncertainties defined by the 16th and 84th percentiles of the distribution. For optical-optical lag analysis, the CCF was evaluated in a lag range of -30 to 30 days. In the case of optical-MIR lags, we adopted a broader lag search range from -200 to 600 days. For estimating lags between optical and MIR wavelengths, the *ZTF* r -band light curve was adopted as the reference because it contains the largest number of data points among the optical bands. In addition, lags between the *WISE W1* and *W2* bands were measured with a lag search range of -600 to 600 days. Lag measurements for a representative RQ-NLSy1, J122844.81+501751.2, are shown in Figs. 7, 8, while the corresponding plots for the remaining sources are presented in the Appendix (see Figs. A.1 to A.3).

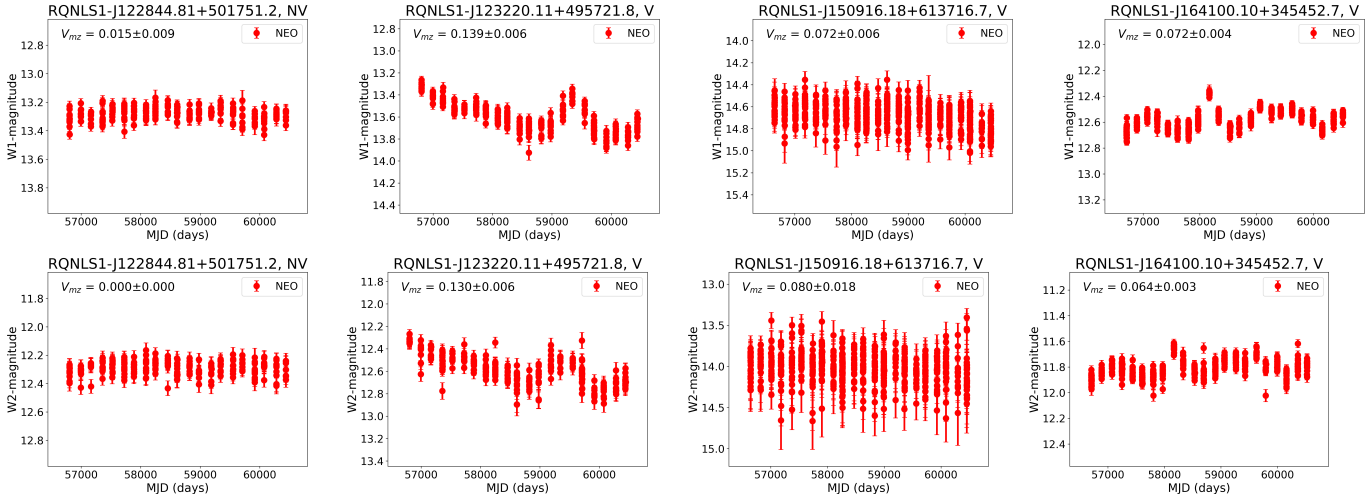


Fig. 2: Long-term *WISE* *W1* and *W2* light curves for the RQ-NLSy1s *J122844.81+501751.2*, *J123220.11+495721.8*, *J150916.18+613716.7*, and *J164100.10+345452.7* from the current sample, which have reliable MIR measurements. All sources exhibit significant variability in both bands, except for *J122844.81+501751.2*, which shows no clear long-term variation. The name and long-term variability status of each source are indicated in the title of each panel, and the estimated redshift-corrected intrinsic variability amplitude, V_{mz} , is shown in the upper-left corner.

Table 2: Variability statistics for the seven radio-quiet narrow-line Seyfert 1 in the optical *g*, *r*, and *i* bands, along with in the mid-infrared *W1* and *W2* bands.

RQ-NLSy1 name	ZTF band	Optical wavelength					Mid-infrared wavelength			
		Time (in days)	Light curve dpts [†]	F_{AGN} values	Status type	$\psi_{pp} \pm \Delta(\psi_{pp})$	$F_{var} \pm \Delta(F_{var})$	<i>WISE</i> band	$V_{mz} \pm \Delta(V_{mz})$	Status type
J102906.69+555625.2	<i>g</i>	2259.963	610	4.650	V	1.026 ± 0.087	0.858 ± 0.018			
J102906.69+555625.2	<i>r</i>	2244.980	927	3.056	V	0.818 ± 0.084	0.623 ± 0.014			
J122844.81+501751.2	<i>g</i>	2285.926	675	1.353	V	0.337 ± 0.046	0.146 ± 0.009	<i>W1</i>	0.015 ± 0.009	NV
J122844.81+501751.2	<i>r</i>	2266.055	754	1.968	V	0.262 ± 0.033	0.178 ± 0.007	<i>W2</i>	0.000 ± 0.000	NV
J122844.81+501751.2	<i>i</i>	1737.042	217	1.642	V	0.234 ± 0.031	0.142 ± 0.012			
J123220.11+495721.8	<i>g</i>	2285.926	695	35.168	V	0.840 ± 0.028	0.907 ± 0.006	<i>W1</i>	0.139 ± 0.006	V
J123220.11+495721.8	<i>r</i>	2266.055	760	31.541	V	0.791 ± 0.026	0.809 ± 0.005	<i>W2</i>	0.130 ± 0.006	V
J123220.11+495721.8	<i>i</i>	1737.042	221	22.238	V	0.558 ± 0.027	0.708 ± 0.010			
J150916.18+613716.7	<i>g</i>	2286.953	1948	3.682	V	0.872 ± 0.077	0.656 ± 0.009	<i>W1</i>	0.072 ± 0.006	V
J150916.18+613716.7	<i>r</i>	2292.040	2161	3.319	V	0.537 ± 0.050	0.403 ± 0.006	<i>W2</i>	0.080 ± 0.018	V
J150916.18+613716.7	<i>i</i>	2205.954	755	3.382	V	0.411 ± 0.039	0.402 ± 0.008			
J151020.06+554722.0	<i>g</i>	2287.829	1098	2.304	V	0.609 ± 0.064	0.384 ± 0.010			
J151020.06+554722.0	<i>r</i>	2284.894	1145	6.695	V	0.519 ± 0.033	0.435 ± 0.005			
J151020.06+554722.0	<i>i</i>	1638.737	380	9.256	V	0.465 ± 0.026	0.426 ± 0.008			
J152205.41+393441.3	<i>g</i>	2286.829	1003	9.183	V	0.529 ± 0.026	0.422 ± 0.005			
J152205.41+393441.3	<i>r</i>	2285.922	1029	28.898	V	0.500 ± 0.015	0.484 ± 0.003			
J152205.41+393441.3	<i>i</i>	1767.048	235	32.125	V	0.514 ± 0.016	0.546 ± 0.006			
J164100.10+345452.7	<i>g</i>	2285.864	1345	4.281	V	0.510 ± 0.039	0.382 ± 0.006	<i>W1</i>	0.072 ± 0.004	V
J164100.10+345452.7	<i>r</i>	2290.946	1387	12.938	V	0.438 ± 0.020	0.391 ± 0.003	<i>W2</i>	0.064 ± 0.003	V
J164100.10+345452.7	<i>i</i>	2210.971	229	14.877	V	0.383 ± 0.018	0.396 ± 0.007			

Data is not available. [†]Number of data points in the optical band light curve. V: Variable; NV: Non-variable.

Table 3: Number of optically variable epochs and total number of epochs of seven radio-quiet narrow-line Seyfert 1 galaxies on different time scales.

Sources	Intranight	Week-like	Month-like	Year-like
J102906.69+555625.2	NO (g, r)	NO (g, r)	YES (g[1/41], r[0/41])	YES (g[1/1], r[1/1])
J122844.81+501751.2	NO (g, r, i)	NO (g, r, i)	YES (g[0/41], r[0/35], i[1/21])	YES (g[1/1], r[1/1], i[1/1])
J123220.11+495721.8	NO (g, r, i)	NO (g, r, i)	YES (g[2/41], r[1/35], i[0/21])	YES (g[1/1], r[1/1], i[1/1])
J150916.18+613716.7	NO (g, r, i)	YES (g[1/74], r[4/76], i[0/20])	YES (g[1/48], r[3/49], i[2/26])	YES (g[1/1], r[1/1], i[1/1])
J151020.06+554722.0	NO (g, r, i)	YES (g[3/50], r[14/50], i[6/16])	YES (g[6/43], r[23/39], i[6/22])	YES (g[1/1], r[1/1], i[1/1])
J152205.41+393441.3	YES (g[1/10], r[7/13])	YES (g[11/47], r[40/48], i[5/6])	YES (g[35/44], r[37/42], i[16/21])	YES (g[1/1], r[1/1], i[1/1])
J164100.10+345452.7	YES (g[3/13], r[4/20])	YES (g[6/75], r[29/71], i[2/3])	YES (g[11/49], r[43/53], i[15/25])	YES (g[1/1], r[1/1], i[1/1])

'[]' represents [variable sessions/total number of sessions]

Table 4: Duty cycle (DC) and mean peak-to-peak amplitude of variability ($\bar{\psi}_{pp}$) of seven radio-quiet narrow-line Seyfert 1 galaxies on different time scales and in different bands.

Sources	Intranight(DC/ $\bar{\psi}_{pp}$) (%)	Week-like (DC/ $\bar{\psi}_{pp}$) (%)	Month-like (DC/ $\bar{\psi}_{pp}$) (%)
J102906.69+555625.2	0% (g, r)	0% (g, r)	(g[2.02/69.40], r[0/0])
J122844.81+501751.2	0% (g, r, i)	0% (g, r, i)	(g[0/0], r[0/0], i[3.96/25.10])
J123220.11+495721.8	0% (g, r, i)	0% (g, r, i)	(g[4.37/16.90], r[2.35/16.30], i[0/0])
J150916.18+613716.7	0% (g, r, i)	(g[1.40/45.00], r[5.35/31.30], i[0/0])	(g[1.96/30.60], r[5.70/29.17], i[7.05/20.45])
J151020.06+554722.0	0% (g, r, i)	(g[7.31/47.23], r[28.43/25.41], i[37.04/19.71])	(g[13.34/43.27], r[55.06/27.05], i[26.65/21.52])
J152205.41+393441.3	(g[10.91/63.00], r[56.05/17.87])	(g[23.79/24.68], r[84.44/20.48], i[78.23/21.08])	(g[75.66/26.67], r[87.39/25.30], i[78.17/27.88])
J164100.10+345452.7	(g[20.27/37.57], r[14.60/26.68])	(g[8.58/35.57], r[39.92/19.01], i[61.17/12.00])	(g[21.49/33.76], r[79.69/18.86], i[57.21/20.45])

“[]” represents $[\text{DC}(\%) / \bar{\psi}_{pp}(\%)]$, where $\bar{\psi}_{pp}$ was computed by considering only the ψ_{pp} values of variable sub-epochs.

3.5. Broadband Spectral Energy Distribution

Modeling the broadband SED helps us to understand the main physical mechanism responsible for the emission. We have compiled the spectral points from all available bands for all objects in our sample. All sources are detected in near-IR, optical-UV, and X-ray. In a gamma-ray with *Fermi*-LAT, the spectral points are produced, and only a few of them have been detected above 3σ significance, while others have only upper limits. The gamma-ray detection directly implies the presence of a jet in these objects. Additionally, the shape of the broadband SED also resembles that of blazars and other γ -NLSy1s, indicating that their demographics are similar to those of these jetted objects. We modeled the broadband SED with a publicly available leptonic code, JETSET⁷. We first started with a simple model where near-IR and optical-UV are fitted with synchrotron emission, and X-ray and gamma-ray are modeled with synchrotron-self-Compton (SSC). In the case where SSC does not fit well with the data, we included the external photon fields from the broad-line region (BLR), and this significantly improves the fit. The broadband SED fit is shown in Fig. 9, and the corresponding parameters are tabulated in Table 5. Out of 7 objects in our sample, only 6 have the available broadband SED data, and hence, the modeling is done only for those objects. In three sources, a strong accretion disk is observed, which dominates the SED, and the upper limits in gamma-rays put constraints on the model parameters. For modeling, a logarithmic parabola was used with low energy powerlaw branch particle distribution with minimum and maximum energy between γ_{min} and γ_{max} , and has r and s parameters as low-energy spectral index and spectral curvature. The parameter γ_{0-lp} is the reference energy. In most cases, γ_{min} is found to be close to 50 and γ_{max} close to 10^6 , which is very commonly seen in blazars, suggesting the presence of strong jets in these objects as well. The size of the emission region R is kept free in all cases. In an ideal situation, R can be constrained from the variability time scale. The size of the emission region in all cases is found to be on the order of 10^{15} cm, suggesting a compact emission region. Similarly, we also optimized the location of the emission region (R_H). In three cases where R_H is of the order of 10^{16} cm, the SSC+EC fits the high-energy part of the SED. As we know, in most of the AGN or blazars, the size of the BLR is $0.1 - 1$ pc, and hence in these cases, the emission region is located within the BLR, and hence the BLR contribution dominates the gamma-ray SED. In the other three cases, when R_H is of the order of 10^{17} cm, the BLR contributes less and the secondary peak is dominated mostly by the SSC, which is equivalent to the situation where the emission region is located at the outer boundary of the BLR. In a few cases, we also see strong domination of the accretion disk, as mostly seen in FSRQ-type

blazars. We also observed varying magnetic fields (B) in all the cases, and these lie in the range of what is observed in blazars. The viewing angle of all these objects is not known, and hence it was optimized during the fitting. We observed a range between 1 and 7 degrees. The bulk Lorentz factor (Γ) is also optimized to obtain the best fit, and is found between 6 and 23, suggesting that the jet flow in RQ-NLSy1s is similar to blazars. The redshift (z) of all sources is fixed to their nominal value. We have also included the contribution of the accretion disk, which is controlled by the luminosity of the accretion disk (L_{disk}) and the temperature (T_{disk}). This lies much below the nominal value of a blazar.

X-ray detection in all these sources is very important as it plays an important role in constraining the model, mostly the SSC part. It also decides whether these objects look more like low synchrotron peak (LSP) blazars or high synchrotron peak (HSP) blazars. In the case where the X-ray lies in the secondary peaks, mostly representing the LSP, compared to other objects where it lies in the synchrotron peak, which represents the case of HSP. In most of the other objects, the X-ray lies in the transition region, representing a sample of intermediate synchrotron peak (ISP) blazars. The magnetic field in all the cases is optimized and found to be between 0.04 and 2.25 Gauss, as mostly seen in other classes of blazars. The viewing angle and Γ of these objects are not known, and therefore they were kept free, but the modeled values come closer to the blazars (see Table 5). The accretion disk contribution is also included to estimate the external Compton from the disk, but it is found to be very subdominant. The overall broadband SED modeling suggests that these objects host relativistic jets and belong to the jetted class of AGN.

4. Results

4.1. Multi-band optical and mid-infrared variability

We investigated flux and color variability in a sample of seven RQ-NLSy1s using optical and mid-infrared light curves. The optical analysis is based on high-cadence *ZTF* observations in the g , r , and i bands, complemented by *WISE* W1 and W2 band data at the MIR wavelength. The presence of intrinsic optical variability was first assessed using the F_{AGN} -test (Equation 1), applied independently to the light curves of g -, r - and i -band. All sources show statistically significant variability on long timescales. The variability amplitude was then quantified using ψ_{pp} and F_{var} , calculated using Equations 2 and 3, respectively. The median ψ_{pp} values are 0.609, 0.519 and 0.438 in the g , r and i bands, while the corresponding median F_{var} values are 0.422, 0.435 and 0.411 (see Table 2). For all sources, ψ_{pp} decreases systematically toward longer wavelengths, with $\psi_{pp}^g > \psi_{pp}^r > \psi_{pp}^i$, except for J152205.41+393441.3, where $\psi_{pp}^r < \psi_{pp}^i$. A similar wavelength-dependent trend in F_{var} is observed

⁷ <https://jetset.readthedocs.io/en/1.3.0/index.html>

Table 5: Broadband SED fitting results. All sources are modeled with *JETSET*, and their corresponding parameters are listed here. The corresponding best fit result is shown in Fig. 9.

Object	J102906.6+555625.2	J122844.8+501751.2	J123220.1+495721.8	J150916.1+613716.7	J151020.0+554722.0	J164100.1+345452.7
γ_{\max}	51.11	50.10	37.39	25.10	57.09	437.94
γ_{\min}	2.79×10^6	1.9×10^6	1.27×10^6	1.44×10^6	7.43×10^6	9.74×10^5
$N [\text{cm}^{-3}]$	5.42×10^3	2.48×10^3	5.51×10^3	3.42×10^3	5.25×10^3	6.29×10^2
γ_{0-lp}	5.18×10^4	1.05×10^4	1.67×10^4	3.10×10^4	2.65×10^3	2.93×10^5
s	2.56	3.59	3.24	2.62	3.54	4.00
r	4.89	2.65	6.98	6.99	1.00	1.03
$R [\text{cm}]$	6.05×10^{15}	5.41×10^{15}	6.43×10^{15}	3.89×10^{15}	2.92×10^{15}	5.65×10^{15}
$R_H [\text{cm}]$	7.31×10^{17}	1×10^{16}	1.08×10^{17}	1.07×10^{16}	1.06×10^{16}	8.61×10^{17}
$B [\text{G}]$	0.04	1.80	1.86	0.37	2.25	1.29
$\theta [\text{degree}]$	1.06	2.92	4.97	2.42	2.99	6.99
Γ	18.26	12.39	8.63	11.55	6.18	22.79
z	0.45	0.26	0.26	0.20	0.15	0.16
$L_{\text{disk}} [\text{erg/s}]$	–	2.58×10^{43}	5.62×10^{44}	1×10^{43}	5.62×10^{43}	3.19×10^{44}
$T_{\text{disk}} [\text{K}]$	–	5.76×10^3	1.8×10^4	3.28×10^4	2.39×10^3	2.67×10^3

The tabulated parameters, γ_{\min} , γ_{\max} , γ_{0-lp} , r , and s are related to the particle distribution. N is the particle number density. R and R_H are the size and the location of the emitting zone. B is the magnetic field. θ , Γ , and z are the viewing angle, the bulk Lorentz factor, and the redshift, respectively.

L_{disk} and T_{disk} are the accretion disk luminosity and temperature, respectively.

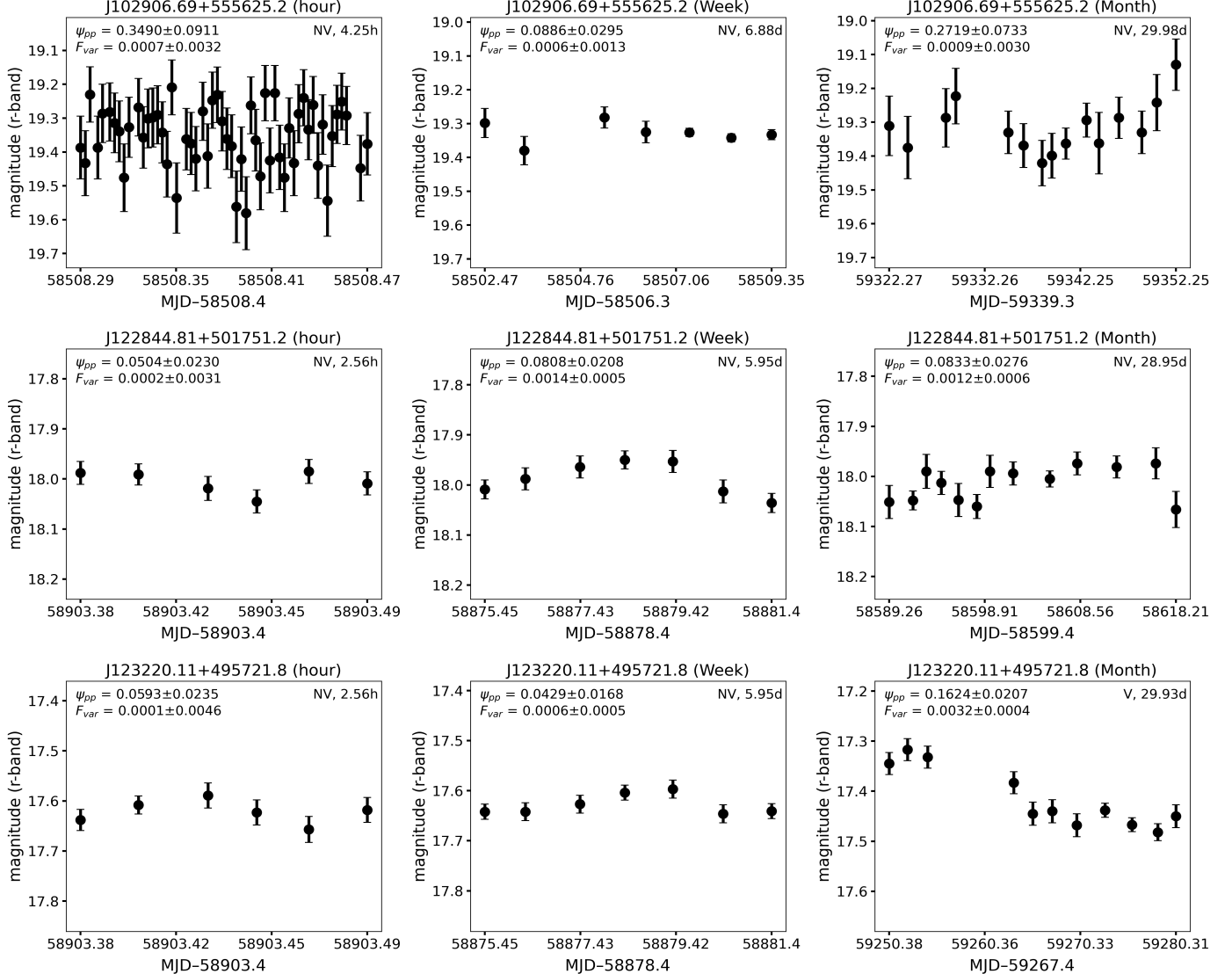


Fig. 3: *ZTF* r-band light curves of the RQ-NLSy1s *J102906.69+555625.2*, *J122844.81+501751.2*, and *J123220.11+495721.8* from the current sample, covering intra-night to month-like timescales. All sources exhibit significant non-variability (NV) on all timescales except for *J123220.11+495721.8*, which shows variability only on month-like timescales. The name and analyzed timescale for each source are given in the panel title. Estimated variability parameters, ψ_{pp} and F_{var} , along with the variability status and duration of each light curve, are indicated in the upper-left and upper-right corners of the respective panels.

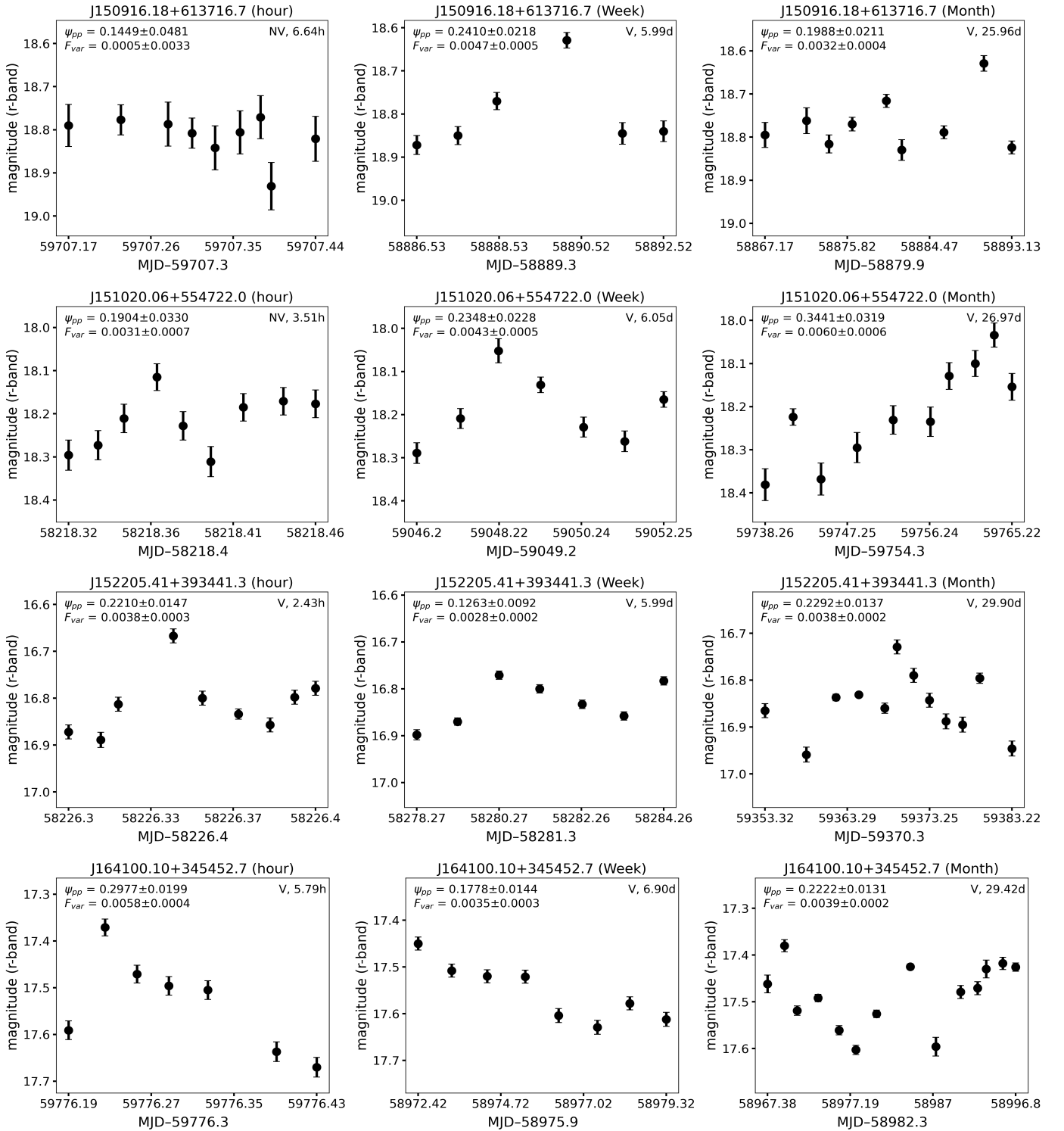


Fig. 3: (Continued) Same as Fig. 3 but for RQ-NLSy1s J150916.18+613716.7, J151020.06+554722.0, J152205.41+393441.3, and J164100.10+345452.7, respectively. All four sources are exhibiting variability on all timescales except for RQ-NLSy1s J150916.18+613716.7 and J151020.06+554722.0, which do not show variability on the intra-night timescale.

for three objects, J102906.69+555625.2, J123220.11+495721.8, and J150916.18+613716.7 (see, Table 2).

Given the high cadence of *ZTF* observations in the *g*, *r*, and *i* bands, we searched for flux variability in the seven RQ-NLSy1s on day-like (intra-night), week-like, and month-like timescales. The *g*-, *r*- and *i*-band light curves were binned at 2-minute, half-day, and one-day intervals and subdivided into independent

sub-epochs spanning half a day, seven days, and 30 days, respectively. This approach yielded multiple sub-epochs for each source on all investigated timescales. To ensure statistical robustness, only sub-epochs containing at least five data points were retained for further analysis; a criterion satisfied by several sub-epochs in each category is tabulated in Table 3. Compared with the *i*-band light curves, this condition is met more frequently in

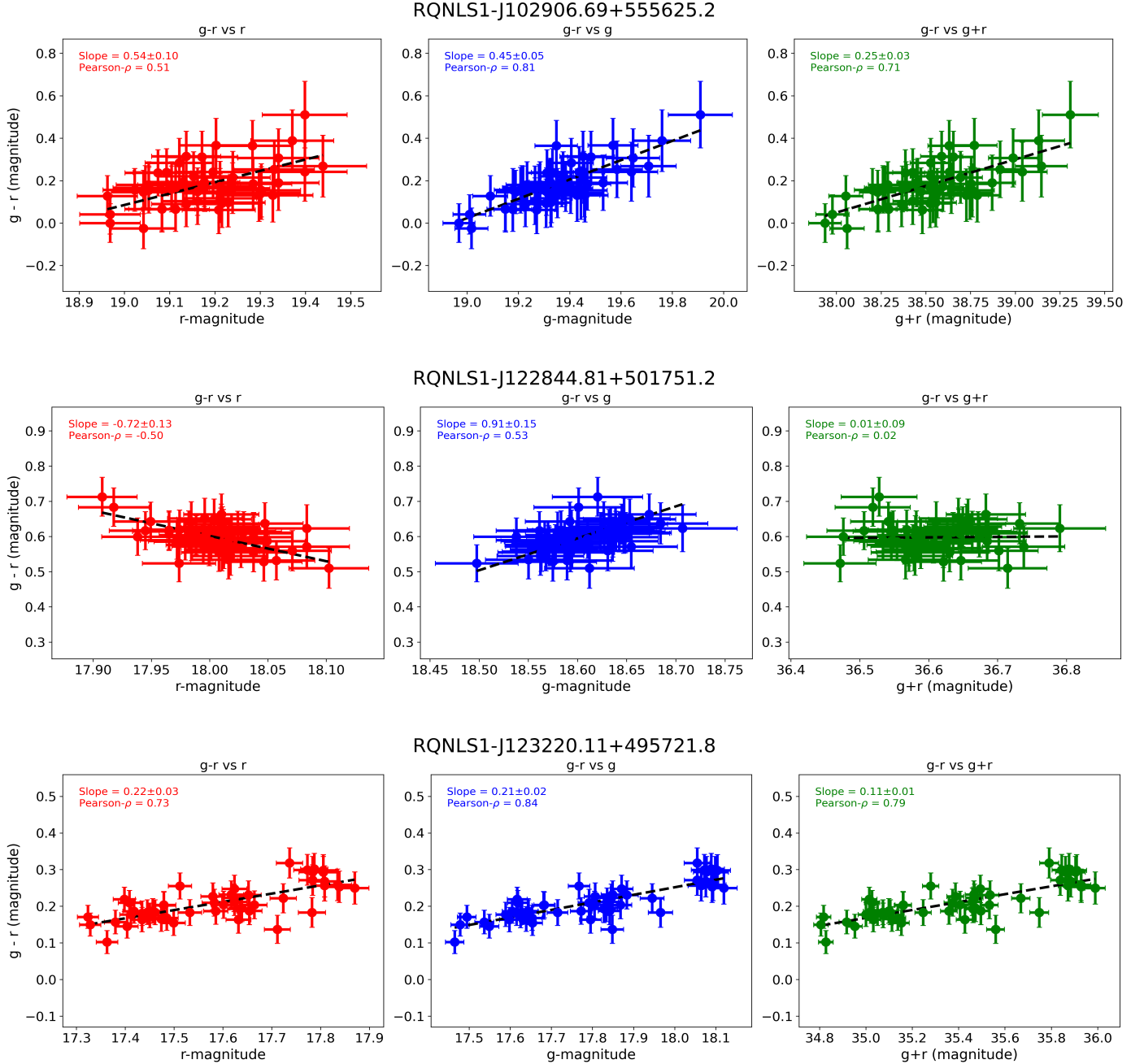


Fig. 4: Long-term ($g-r$) color variations versus r -magnitude, g -magnitude, and $(g+r)$ for the RQ-NLSy1s $J102906.69+555625.2$ (top), $J122844.81+501751.2$ (middle), and $J123220.11+495721.8$ (bottom) from the current sample. Significant positive trends are observed in $J102906.69+555625.2$ and $J123220.11+495721.8$ across all color-magnitude combinations. The black dashed line shows the best fit obtained using orthogonal distance regression, accounting for uncertainties in both color and magnitude. The corresponding slope and Pearson- ρ are indicated in the upper-left corner of each panel.

the g and r bands, likely reflecting the lower observational cadence of the *ZTF* i -band data. We, therefore, restrict the short- and intermediate-timescale variability analysis to the g - and r -band light curves.

All retained sub-epochs were subjected to the variability tests described in Sect. 3.1, and the number of variable and total sub-epochs was determined for each source and investigated timescales. The corresponding statistics are listed in Table 3. Using these results, we compute the DC for each source. In most cases, the DC is higher in the r band than in the g band,

except for $J164100.10+345452.7$ on intra-night timescales and $J102906.69+555625.2$ and $J123220.11+495721.8$ on month-like timescales. Despite this, the mean peak-to-peak variability amplitude ($\bar{\psi}_{pp}^g$) consistently satisfies $\bar{\psi}_{pp}^g > \bar{\psi}_{pp}^r$ on all examined timescales. DC and $\bar{\psi}_{pp}$ are summarized for each source in Table 4.

Unlike optical analysis, MIR variability could be examined for only four of the seven sources, as these sources retain reliable *WISE* $W1$ and $W2$ band measurements after applying the

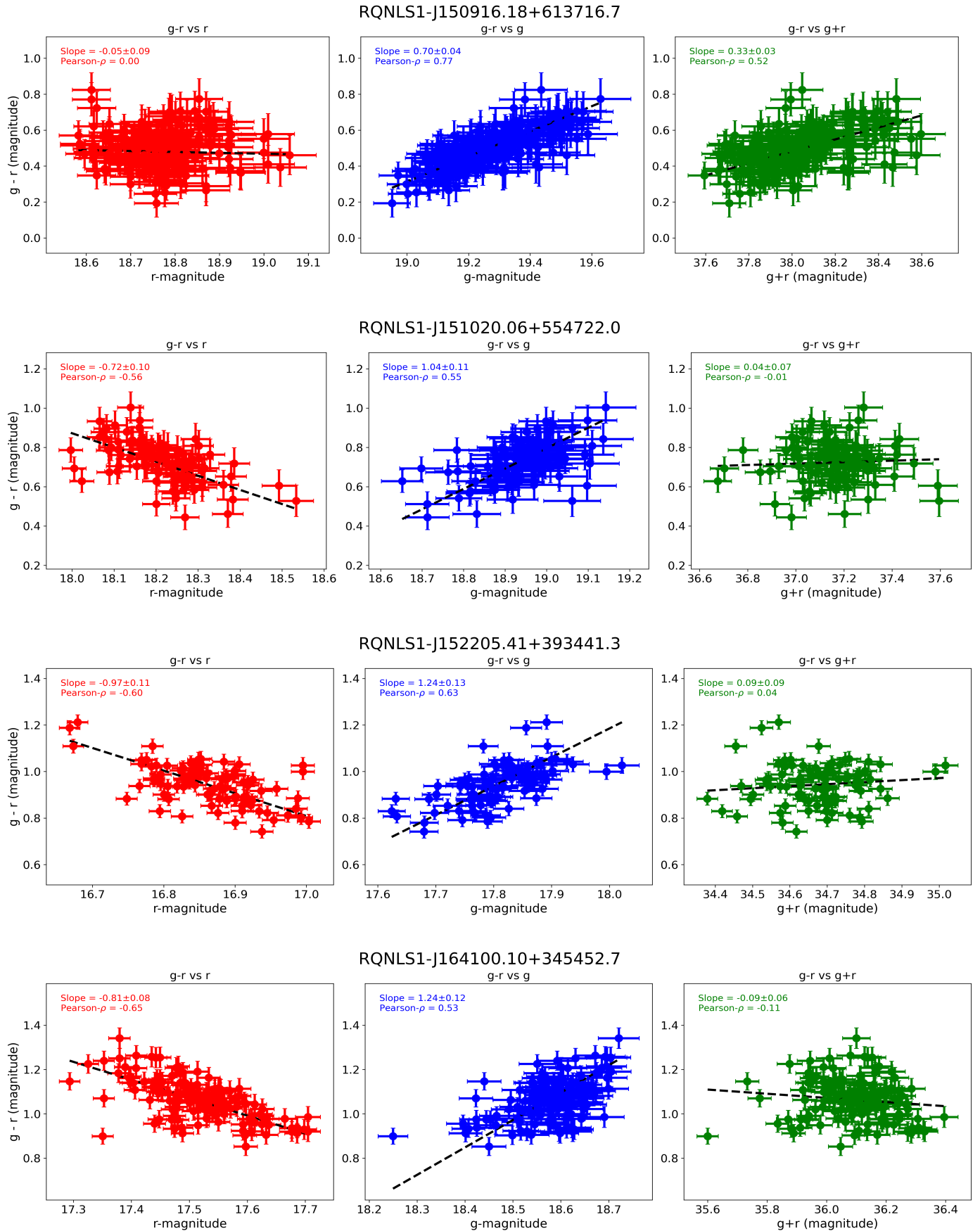


Fig. 4: (Continued) Same as Fig. 4 but for RQ-NLSy1s J150916.18+613716.7, J151020.06+554722.0, J152205.41+393441.3, and J164100.10+345452.7, respectively, presented from the top to bottom. Only J150916.18+613716.7 showed a significant positive trend in its $g-r$ versus $g+r$ color-magnitude diagram.

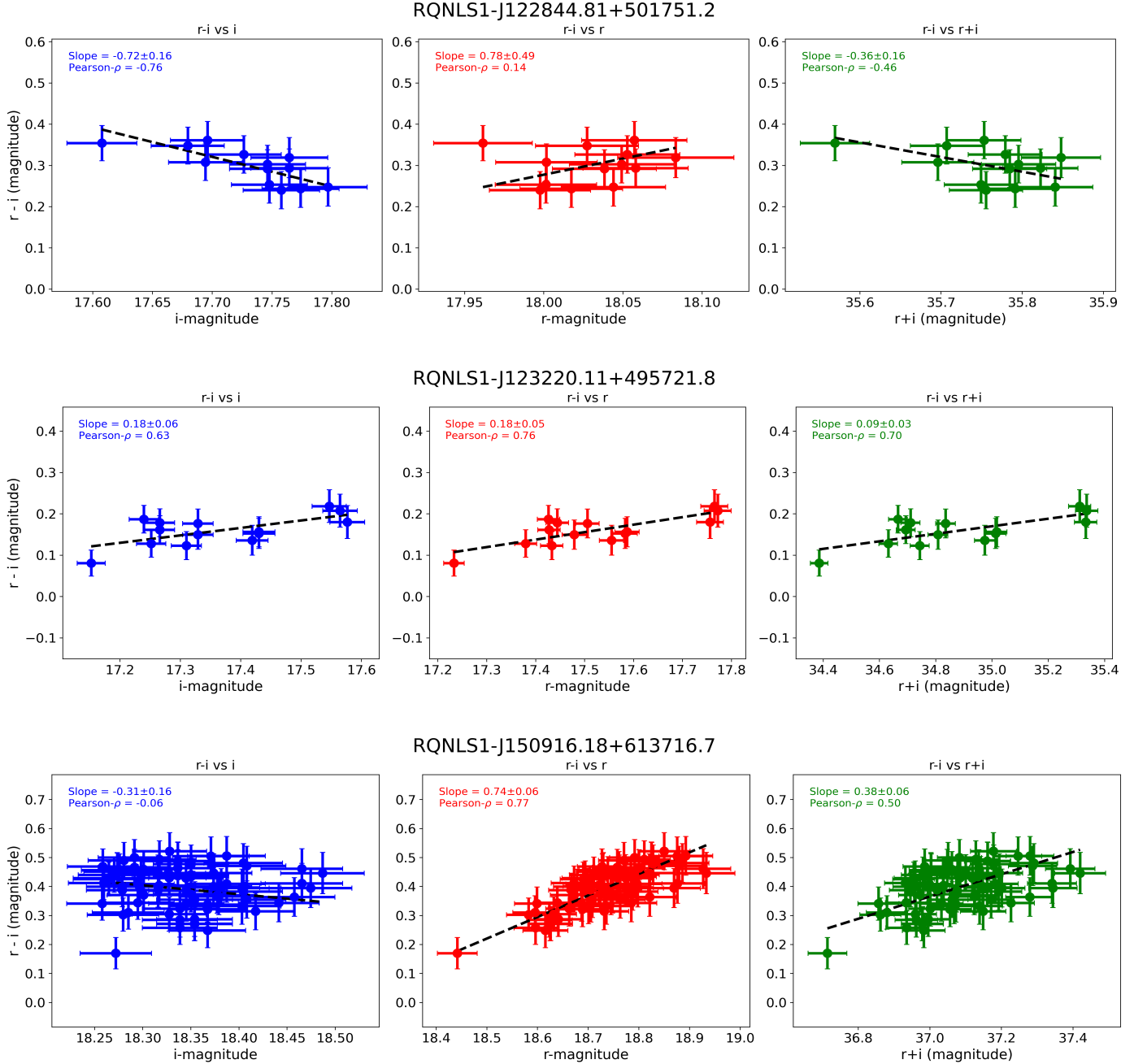


Fig. 5: Same as Fig. 4 but for the log-term ($r-i$) color variations versus i -magnitude, r -magnitude, and $(r+i)$ for the RQ-NLSy1s $J122844.81+501751.2$ (top), $J123220.11+495721.8$ (middle), and $J150916.18+613716.7$ (bottom) from the current sample. Significant positive trends are observed in $J123220.11+495721.8$ and $J150916.18+613716.7$ from their $r-i$ versus $r+i$ color-magnitude diagrams.

selection criteria described in Sect. 2.2. The presence of intrinsic MIR variability was assessed by computing the redshift-corrected rest-frame intrinsic variability amplitude (V_{mz}) using Equation 7. Of the four sources, three satisfy our adopted variability criterion of $V_{mz} \gtrsim 0.1$ within the associated uncertainties in both $W1$ and $W2$ bands, indicating statistically significant MIR variability. The corresponding values of V_{mz} for individual sources are reported in Table 2.

4.2. Optical and mid-infrared color variability

As discussed in Sect. 3.3, the inferred color-magnitude trend can reverse when the shorter-wavelength (bluer) magnitude is placed on the horizontal axis therefore, following Ojha et al. (2025), we base our analysis on the color-magnitude diagrams ($m_1 - m_2$) versus $(m_1 + m_2)$, where this effect is properly mitigated. Based on the optical color-magnitude diagrams, a statistically significant BWB trend is detected in three of the seven RQ-NLSy1s, namely $J102906.69+555625.2$, $J123220.11+495721.8$, and $J150916.18+613716.7$ (see Fig. 4). The remaining four

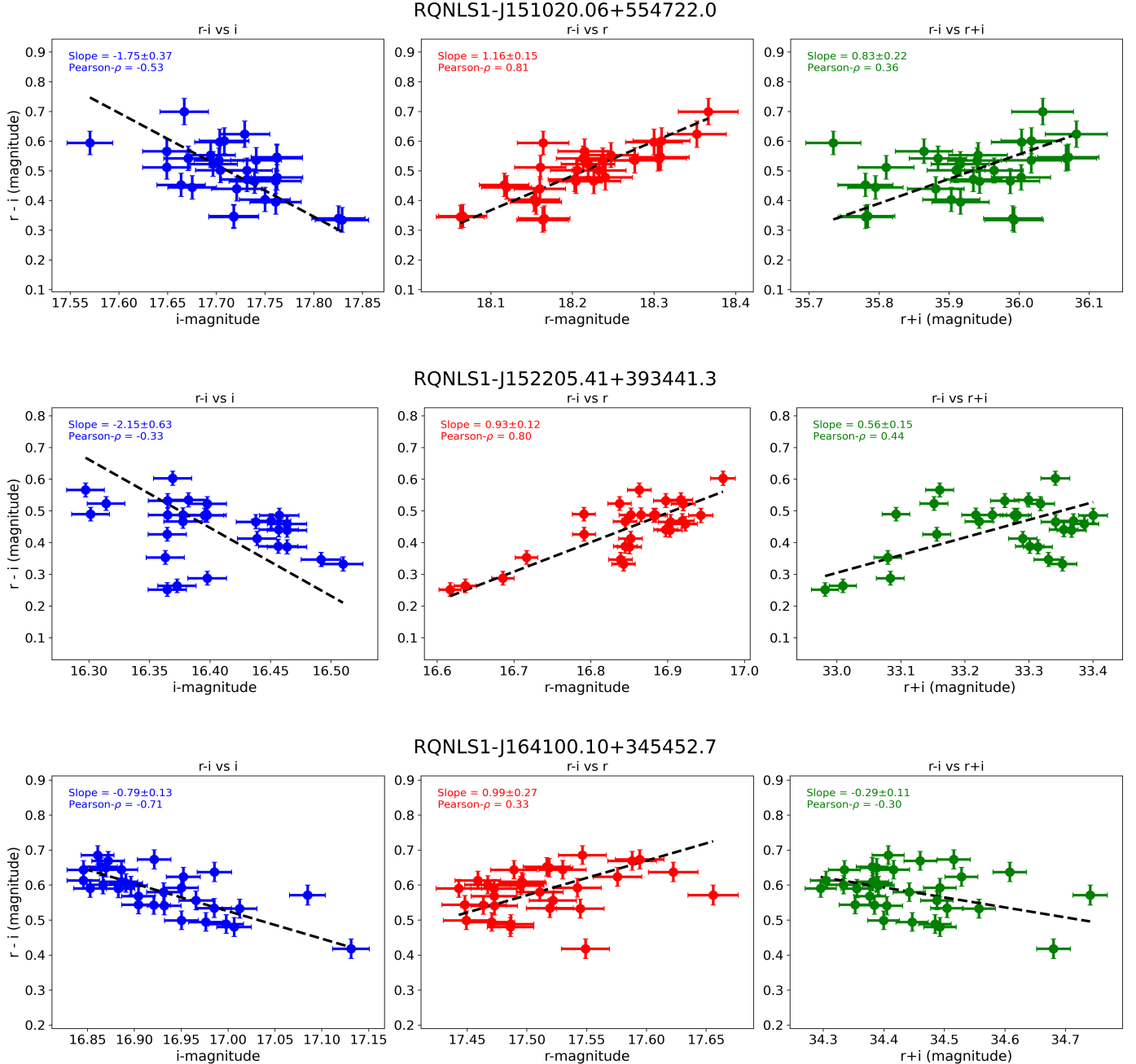


Fig. 5: (Continued) Same as Fig. 5 but for RQ-NLSy1s *J151020.06+554722.0* (top), *J152205.41+393441.3* (middle), and *J164100.10+345452.7* (bottom), respectively. All these sources did not show a significant trend from their $r-i$ versus $r+i$ color-magnitude diagrams.

sources do not show significant correlations and are therefore classified as NOT. Consistent results are obtained when the analysis is repeated using *ZTF* r and i band data (see Fig. 5). We applied the same methodology to investigate the color variability at MIR wavelengths. Among the four sources with reliable *WISE* data, only *J150916.18+613716.7* exhibits a statistically significant RWB trend, while the remaining sources do not (see Fig. 6).

4.3. Intra- and inter-band lag measurements

Motivated by the pronounced continuum variability and color behavior discussed in Sects. 4.1 & 4.2, we used the high-

cadence *ZTF* observations to investigate wavelength-dependent time delays within the optical regime. The ICCF method, described in Sect. 3.4, was applied to each RQ-NLSy1 in the sample, adopting the g band as the reference continuum. Optical intra-band lags were measured by cross-correlating the r - and i -band light curves with the g -band light curve. The ICCF results for *J123220.11+495721.8* are shown in Fig. 7, while those for the remaining six sources are presented in Figs. A.1 and A.2. Adopting a conservative threshold of the maximum correlation coefficient (R_{\max}) > 0.6 to identify reliable correlations, we find no statistically significant optical intra-band lags within the associated uncertainties for any of the targets except

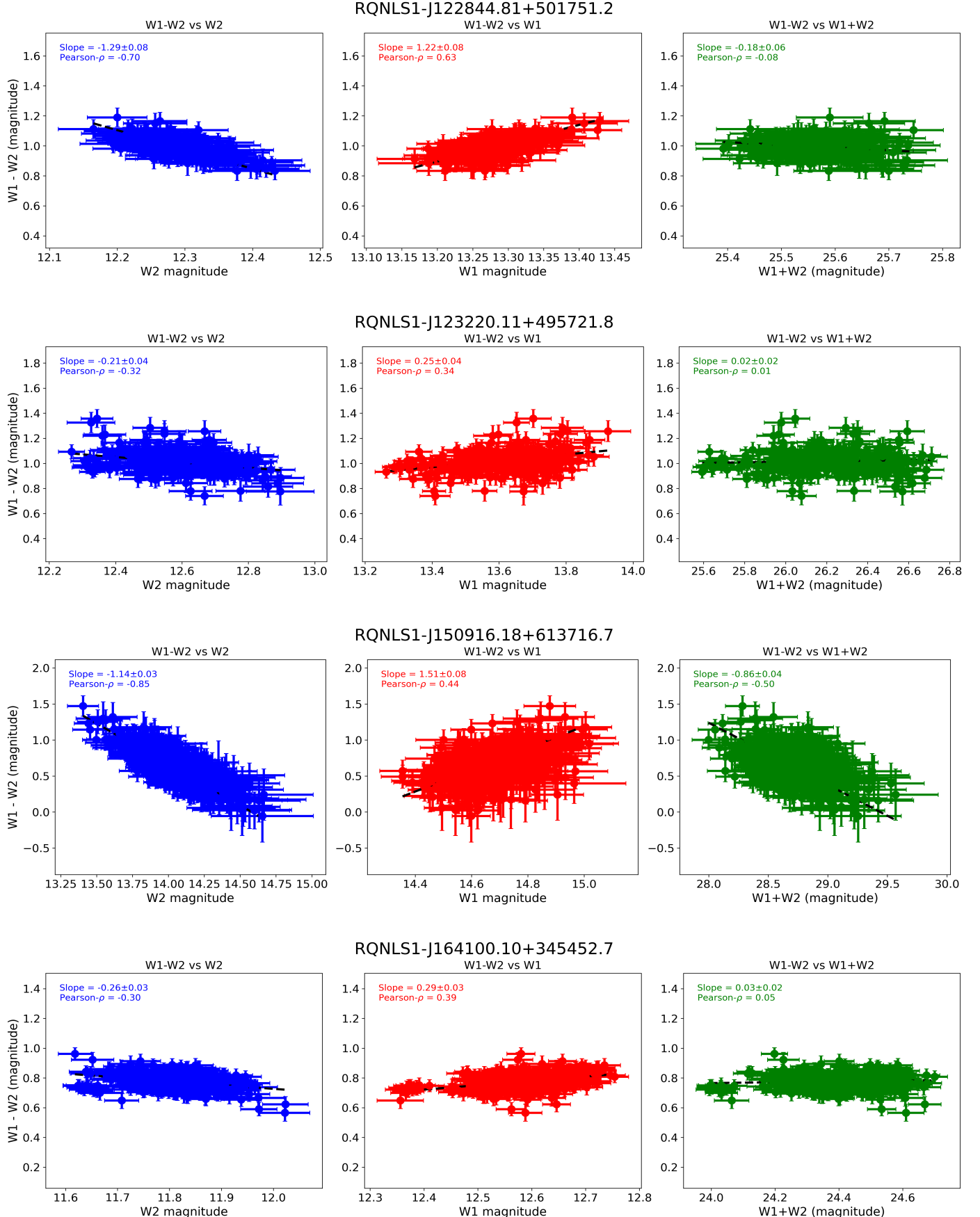


Fig. 6: Same as Fig. 4 but for the log-term ($W1-W2$) color variations versus $W2$ -magnitude, $W1$ -magnitude, and $(W1+W2)$ for the RQ-NLSy1s $J122844.81+501751.2$, $J123220.11+495721.8$, $J150916.18+613716.7$, and $J164100.10+345452.7$, respectively, presented from the top to bottom. Out of four sources, only $J150916.18+613716.7$ showed a significant negative trend from its $W1-W2$ versus $W1+W2$ color-magnitude diagram.

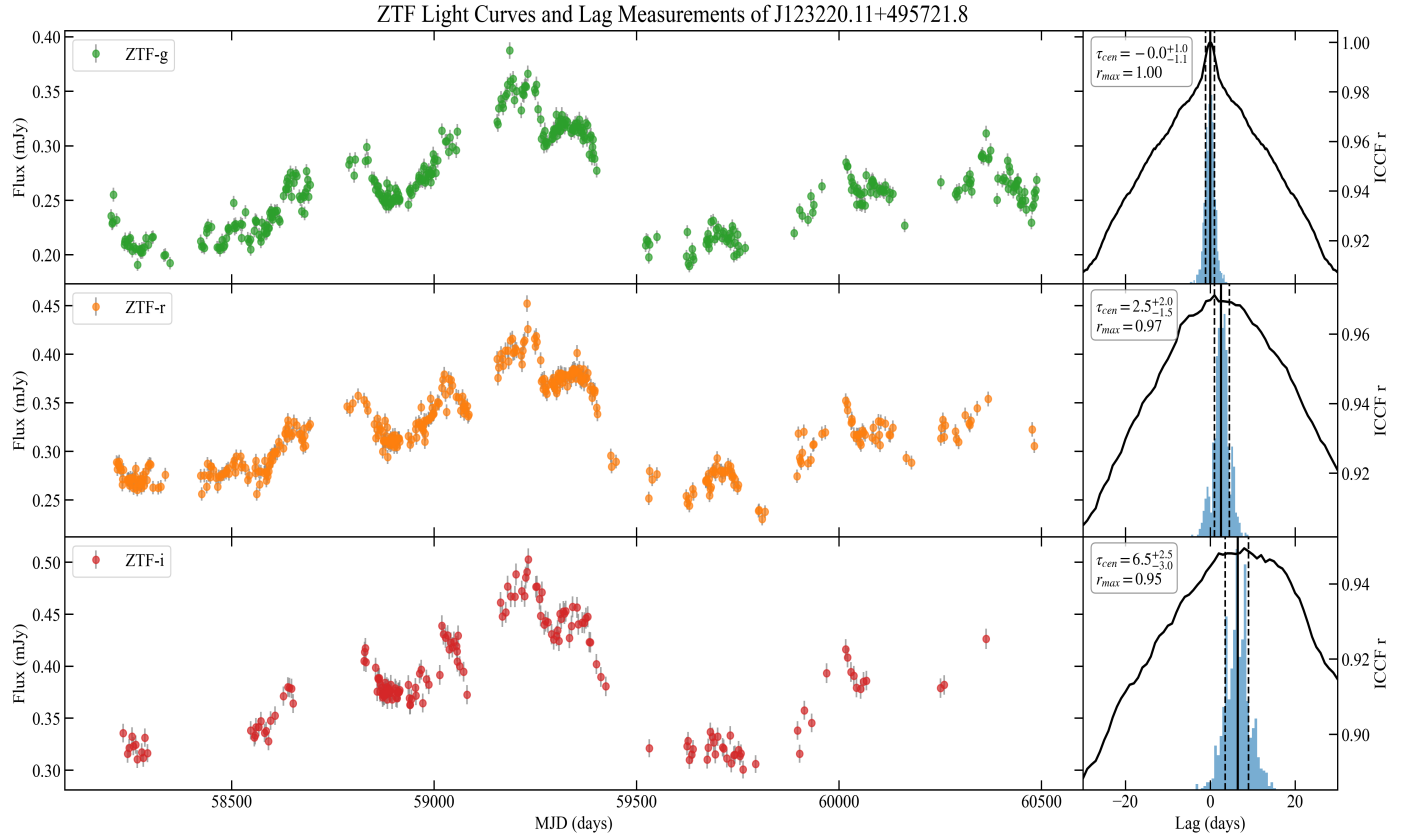


Fig. 7: The *ZTF* light curves and lag measurements for the source J123220.11+495721.8. Left panel: The *ZTF* *g*-, *r*-, and *i*-band light curves. Right panel: The cross-correlation functions (in black) and centroid distributions (in blue) for each band relative to the *ZTF* *g* band.

for J123220.11+495721.8, for which a systematic increase in the intra-band lags towards longer wavelength was found (see Fig. 7).

On the other hand, we performed an ICCF analysis for the four sources with available MIR coverage to measure the time lags between the optical *r* band and the MIR *W1* and *W2* bands, as well as between the MIR *W1* and *W2* bands themselves. Among these four sources, three exhibit strong correlations with $r_{\max} > 0.6$. The ICCF results for J123220.11+495721.8 are presented in Fig. 8, while those for the remaining two sources are shown in Fig. A.3. Throughout this work, a positive lag indicates that variability in the shorter-wavelength band leads to the longer-wavelength band. In the following, we describe the results of the continuum optical to mid-infrared inter-band and MIR intra-band lag measurements for these three RQ-NLSy1s.

RQ-NLSy1 J123220.11+495721.8: For this source, the ICCF analysis yields highly significant centroid inter-band lags between the optical and MIR light curves. The *ZTF* *r*-band variations lead those in the *WISE* bands by $\tau_{\text{centroid}}^{r-W1} = 188.6^{+75.2}_{-48.3}$ days and $\tau_{\text{centroid}}^{r-W2} = 266.4^{+91.1}_{-79.5}$ days, with corresponding $R_{\max} = 0.85$ and 0.77, respectively, indicating robust optical–MIR correlations. A strong MIR intra-band correlation is also detected between the *WISE* *W1* and *W2* light curves, with a centroid lag of $\tau_{\text{centroid}}^{W1-W2} = 29.4^{+81.3}_{-75.2}$ days and $R_{\max} = 0.98$, representing the most significant MIR intra-band lag among the three sources with reliable measurements. The ICCF lag analysis for this source is shown in Fig. 8. Using these measured lags, we estimate that the upper limit of characteristic distance of the MIR emitting region from the accretion disk is 4.87×10^{17} cm and 6.89×10^{17} cm, and

that the characteristic size of the emitting region at MIR wavelengths is 7.51×10^{16} cm following the relation, $R \sim c\tau_{\text{centroid}}$.

RQ-NLSy1 J150916.18+613716.7: For this source, the ICCF analysis reveals correlated optical-mid-infrared variability, although the inferred centroid lags are weakly constrained due to large uncertainties. The *ZTF* *r*-band light curve leads the *WISE* *W1* and *W2* light curves by $\tau_{\text{centroid}}^{r-W1} = 69.3^{+239.4}_{-114.0}$ days and $\tau_{\text{centroid}}^{r-W2} = 220.1^{+260.6}_{-283.5}$ days, with $R_{\max} = 0.84$ and 0.73, respectively. While the correlation coefficients indicate statistically meaningful correlations, the large uncertainties imply that the inter-band delays are not well constrained. The MIR intra-band analysis between the *WISE* *W1* and *W2* light curves yields a centroid lag of $\tau_{\text{centroid}}^{W1-W2} = -9.6^{+350.0}_{-356.7}$ days with $R_{\max} = 0.66$. This lag is consistent with near-simultaneous variability between the two MIR bands within the uncertainties. The ICCF results for this source are presented in Fig. A.3. Using these measured lags, we estimate that the upper limit of characteristic distance of the MIR emitting region from the accretion disk is 1.79×10^{17} cm and 5.70×10^{17} cm, and that the characteristic size of the emitting region at MIR wavelengths is 2.49×10^{16} cm.

RQ-NLSy1 J164100.10+345452.7: For J164100.10+345452.7, the ICCF analysis indicates the presence of optical-to-mid-infrared time delays, although the correlations between the optical and MIR bands are comparatively weak. The *ZTF* *r*-band variations lead those in the *WISE* bands by $\tau_{\text{centroid}}^{r-W1} = 289.1^{+163.2}_{-83.7}$ days and $\tau_{\text{centroid}}^{r-W2} = 330.8^{+146.8}_{-116.0}$ days, with $R_{\max} = 0.70$ and 0.60, respectively. These values suggest delayed MIR variability relative to the optical emission, but with comparatively marginal correlation strengths. In contrast,

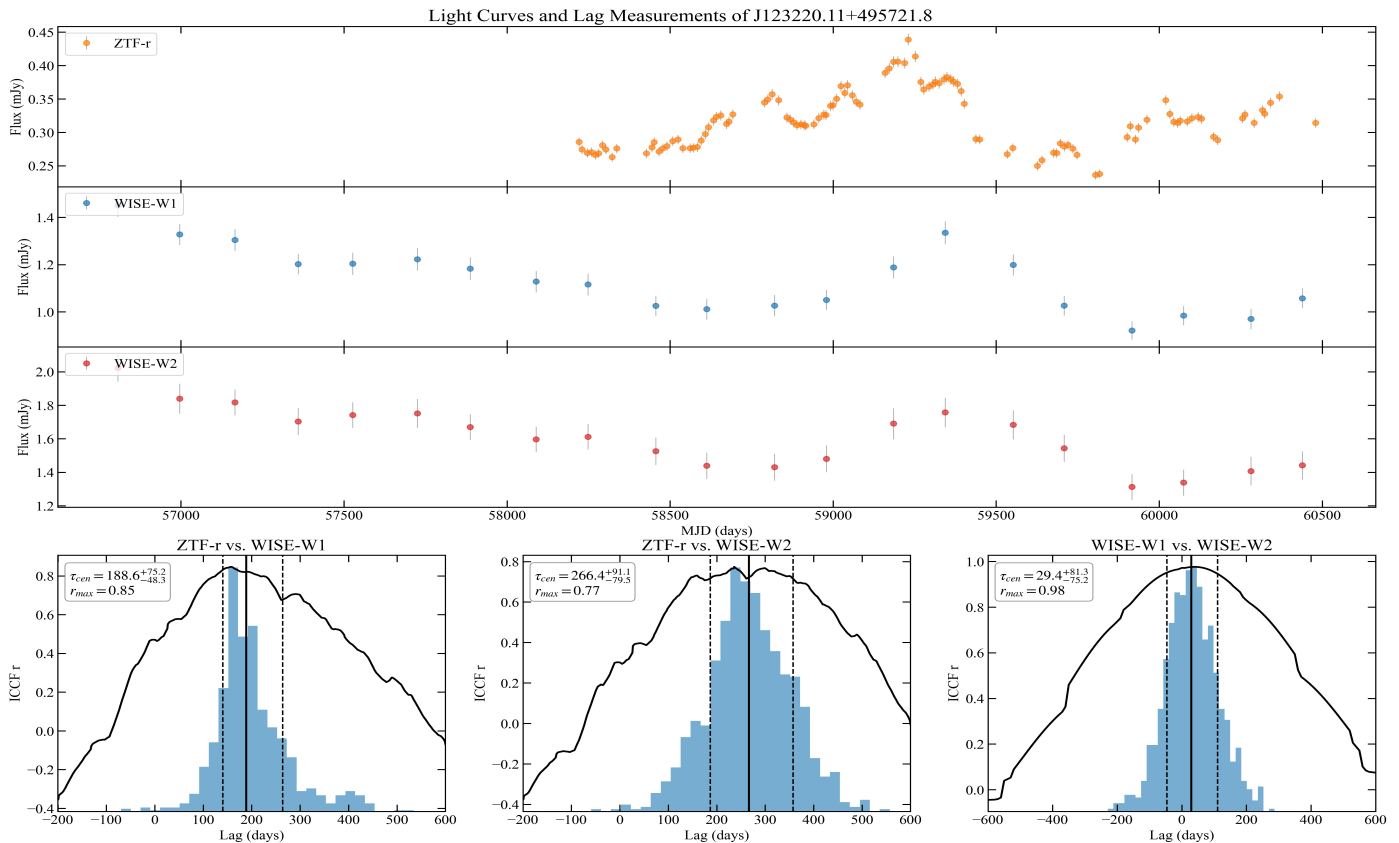


Fig. 8: The *ZTF* and *WISE* binned light curves and lag measurements for the source J123220.11+495721.8. The upper three panels show the binned light curves of *ZTF r* band and *WISE W1*, *W2* bands, while the bottom panel shows the corresponding lag measurements. Panels from left to right correspond to *ZTF r* vs. *WISE W1*, *ZTF r* vs. *WISE W2*, and *WISE W1* vs. *WISE W2*.

a highly significant MIR intra-band lag is detected between the *WISE W1* and *W2* light curves, with a centroid lag of $\tau_{\text{cen}}^{W1-W2} = 20^{+61.2}_{-40.7}$ days with a strong $R_{\text{max}} = 0.96$. The ICCF lag analysis for this source is shown in Fig. A.3. Using these measured lags, we estimate that the upper limit of characteristic distance of the MIR emitting region from the accretion disk is 7.49×10^{17} cm and 8.55×10^{17} cm, and that the characteristic size of the emitting region at MIR wavelengths is 5.18×10^{16} cm.

In all three cases, the characteristic size of the MIR emitting region is measured using the lag between *W1* and *W2* bands. Comparing the location of the MIR emission region with the parameters R_H (location of the emitting region) of the SED modeling result, we suggest that the MIR region can contribute significantly to the broadband SED.

4.4. Dependence of long-term variability amplitude on AGN parameters

To examine the dependence of ψ_{pp} on fundamental AGN properties, we compiled the spectroscopic and physical parameters of the seven RQ-NLSy1s from Crepaldi et al. (2025). The adopted parameters include the Fe II to H β flux ratio (R_{4570}), the [O III] to H β flux ratio (R_{5007}), the average monochromatic flux density at 5100 \AA ($\langle f_{5100,\text{\AA}} \rangle$), the black hole mass (M_{BH}), the average bolometric luminosity ($\langle L_{\text{bol}} \rangle$) and the average Eddington ratio ($\langle R_{\text{Edd}} \rangle$). The underlying spectral analysis was carried out using Gran Telescopio Canarias spectra, as described in Crepaldi et al. (2025).

In this work, we adopt $\langle f_{5100,\text{\AA}} \rangle$ as the average of the flux densities measured from the Gran Telescopio Canarias and SDSS spectra, $\langle L_{\text{bol}} \rangle$ as the average of the measured and derived bolometric luminosities, and $\langle R_{\text{Edd}} \rangle$ as the average of the measured and derived Eddington ratios. The average black hole masses reported in Crepaldi et al. (2025) are used throughout. Since one source (J102906.69+555625.2) lacks *ZTF i*-band coverage, and because the *i*-band light curves have substantially lower cadence than those in the *g* and *r* bands, we restrict this analysis to the *g*- and *r*-band variability amplitudes to maintain uniformity and statistical reliability.

The correlations between ψ_{pp} and the AGN parameters were quantified using the Pearson correlation coefficient, and the results are shown in Fig. 10. We find strong anti-correlations of ψ_{pp} with R_{4570} (Pearson- $\rho = -0.81$), R_{5007} (Pearson- $\rho = -0.74$), and $\langle R_{\text{Edd}} \rangle$ (Pearson- $\rho = -0.54$). A moderate negative correlation is also observed between ψ_{pp} and $\langle f_{5100,\text{\AA}} \rangle$, with Pearson- $\rho = -0.46$. In contrast, a strong positive correlation is found between ψ_{pp} and M_{BH} , with Pearson- $\rho = +0.76$. A weak to mild positive correlation is present between ψ_{pp} and $\langle L_{\text{bol}} \rangle$, with Pearson- $\rho = +0.36$.

5. Discussion

In this article, we investigate the flux and color variability properties of seven peculiar NLSy1 galaxies that exhibit extreme radio characteristics. Our analysis combines a detailed study of optical variability across multiple timescales with a long-term

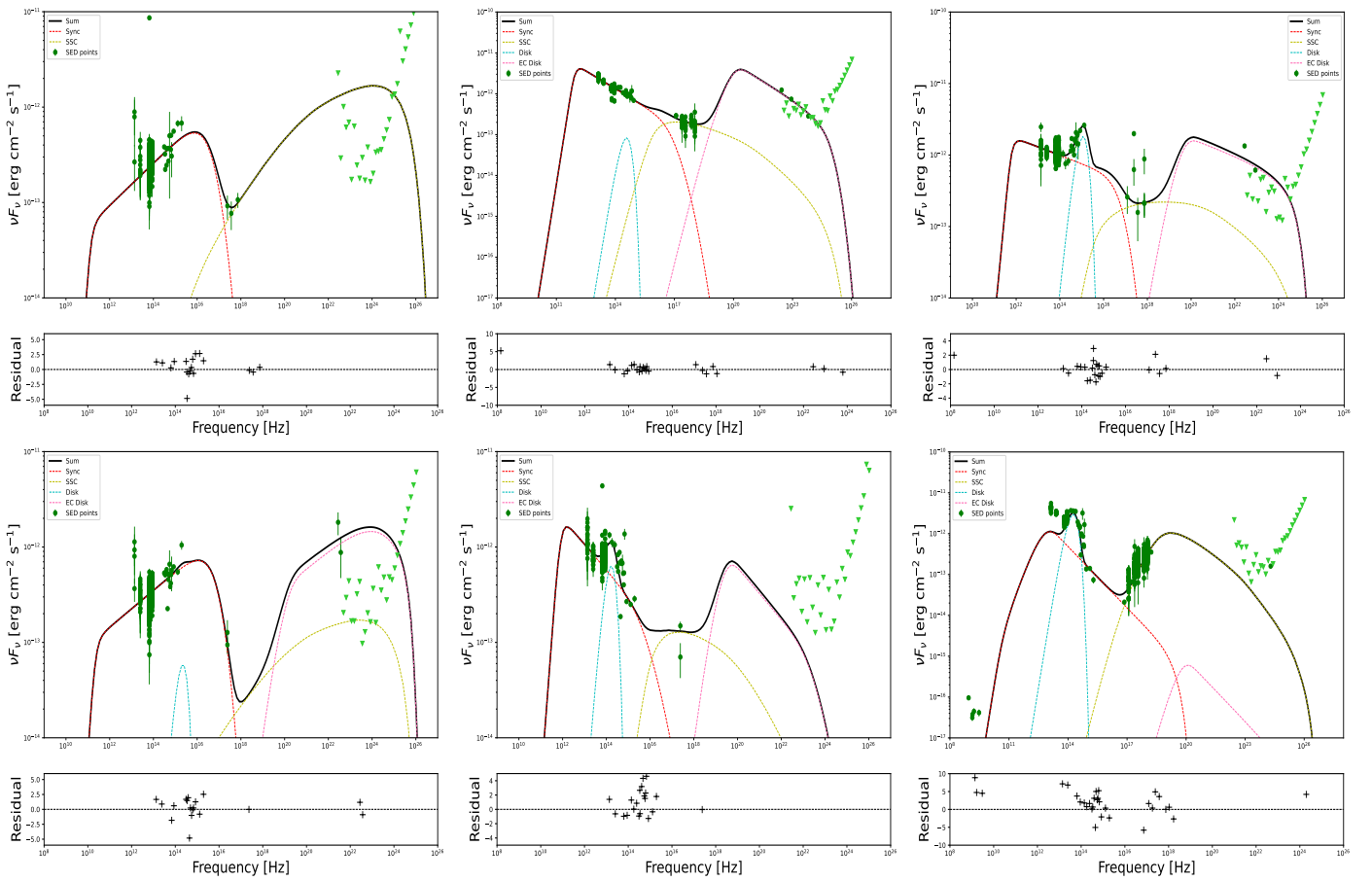


Fig. 9: Spectral Energy Distribution (SED) of six RQ-NLSy1s, and all are modeled with JetSet. *Top left*: SDSS J102906.69+555625.2, *Top middle*: SDSS J122844.81+501751.2, *Top right*: SDSS J123220.11+495721.8, *Bottom left*: SDSS J150916.18+613716.7, *Bottom middle*: SDSS J151020.06+554722.0 *Bottom right*: SDSS J164100.10+345452.7. The best fit parameters are shown in Table 5.

examination of flux and color variability in both the optical and mid-infrared wavelength regimes.

5.1. Flux variability

Table 2 shows that all seven RQ-NLSy1s in our sample exhibit statistically significant variability on long timescales. Such variability may arise from instabilities in the accretion disk (e.g., Wiita et al. 1991; Chakrabarti & Wiita 1993; Mangalam & Wiita 1993) or from fluctuations associated with relativistic jets (e.g., Marscher & Gear 1985; Wagner & Witzel 1995; Marscher 2014). To distinguish between these two possibilities, we applied the variability amplitude criterion proposed by Bauer et al. (2009), adopting a threshold of $\psi \geq 0.4$ mag for the *ZTF* g -, r - and i -band light curves of all seven sources. This criterion yields $\psi_{\text{pp}}^{g, r, i} \geq 0.4$ for five sources, while only four sources also satisfy $F_{\text{var}}^{g, r, i} \geq 0.4$ (see Table 2). The simultaneous fulfillment of both conditions suggests that, among the seven RQ-NLSy1s, four sources are likely to exhibit jet-dominated optical variability. To further test this interpretation, we examined the wavelength dependence of the variability amplitude for these four objects. We find that three sources, J102906.69+555625.2, J123220.11+495721.8, and J150916.18+613716.7, show a systematic decrease in variability amplitude with increasing wavelength, such that $\psi_{\text{pp}}^g > \psi_{\text{pp}}^r > \psi_{\text{pp}}^i$ and $F_{\text{var}}^g > F_{\text{var}}^r > F_{\text{var}}^i$ (see Table 2). The resultant trend can be naturally explained

within the framework of the shock-in-jet model (see Türler 2011), in which particles are accelerated to high energies at the shock front. Because higher-energy electrons undergo more rapid radiative cooling than lower-energy ones, variability amplitudes are expected to be higher at higher observing frequencies (Kirk et al. 1998; Mastichiadis & Kirk 2002). Additionally, Table 2 shows that both the mean peak-to-peak variability $\psi_{\text{pp}}^{g, r, i}$ and the mean fractional variability $F_{\text{var}}^{g, r, i}$, for three RQ-NLSy1s, J102906.69+555625.2, J123220.11+495721.8 and J150916.18+613716.7, are higher than for the remaining four individual sources. This is consistent with previous findings that objects hosting jets tend to display larger amplitudes of optical variability (Rakshit & Stalin 2017). Thus, based on these long-term optical variability properties, we therefore strongly suggest that jet-related processes most plausibly drive the optical variability in three of the seven RQ-NLSy1s in our sample.

On the other hand, among the four RQ-NLSy1s with reliable *WISE* $W1$ and $W2$ band measurements, three sources, J123220.11+495721.8, J150916.18+613716.7, and J164100.10+345452.7, exhibit statistically significant MIR variability. The presence of pronounced variability at MIR wavelengths, where thermal emission from the dusty torus is expected to dominate, provides additional support for a non-thermal contribution, most plausibly associated with jet activity. This mid-infrared variability therefore reinforces the interpretation, based on the optical variability properties, that jet-related processes

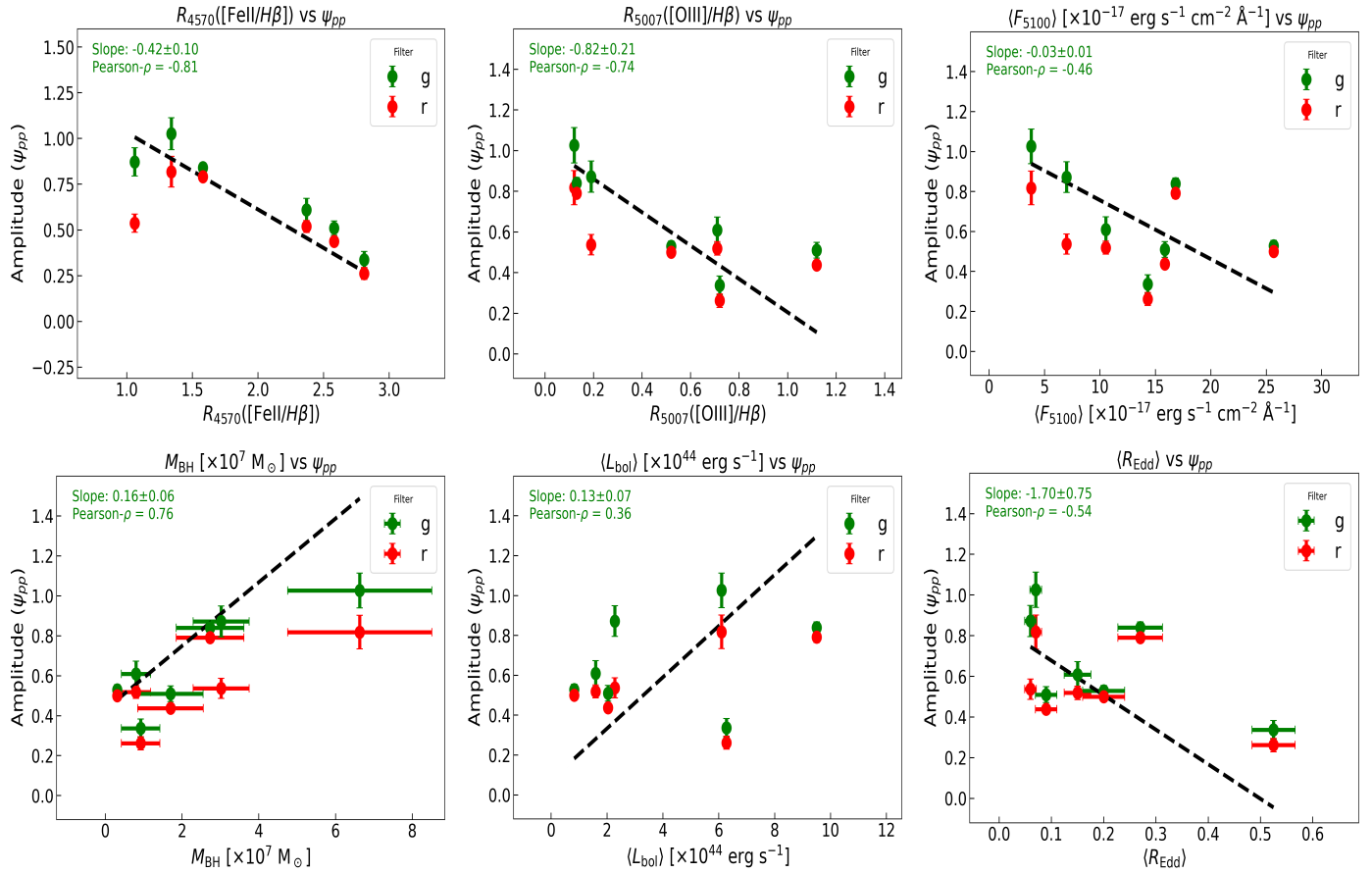


Fig. 10: Figure showing correlation of variability amplitude (ψ_{pp}) with physical parameters of AGN, R_{4570} , R_{5007} , $\langle F_{5100} \text{Å} \rangle$, M_{BH} , $\langle L_{\text{bol}} \rangle$, and $\langle R_{\text{Edd}} \rangle$. The black dashed line represents the best fit obtained using orthogonal distance regression, accounting for uncertainties in both axes parameters. The best-fit linear regression parameters, including the slope and Pearson- ρ , are computed including joined data from ZTF g , and r bands of the seven RQ-NLSy1s and are displayed in the upper-left corner of each panel.

play a significant role in driving the observed long-term variability in a subset of RQ-NLSy1s.

To explore optical variability on sub-timescales, we analyzed high-cadence ZTF g -, r -, and i -band light curves of the seven RQ-NLSy1s, following the strategy described in Sect. 4.1. As summarized in Table 3, three sources, J102906.69+555625.2, J123220.11+495721.8, and J150916.18+613716.7, do not show statistically significant variability on intra-night or week-like timescales in any of the optical bands. The only exception is J150916.18+613716.7, which exhibits weak variability on week-like timescales, with duty cycles of $\sim 1\%$ in the g -band and $\sim 5\%$ in the r -band (see Table 4). When these results are considered together with the recent intra-night optical variability (INOV) study of the same sample by Ojha et al. (2024), a more nuanced picture emerges. In that work, J102906.69+555625.2 and J123220.11+495721.8 were found to exhibit significant INOV, with a DC of $\sim 31\%$ and $\sim 21\%$, respectively. In contrast, INOV was not detected in J150916.18+613716.7 during three observing epochs, each lasting more than 3 hours. Taken together, the results of the present analysis and the earlier INOV study support a jet-related origin for the sub-timescale optical variability in J102906.69+555625.2, J123220.11+495721.8, and J150916.18+613716.7, a conclusion that is further strengthened by their long-term color-variability properties (e.g., see below).

In contrast, although two other sources in the sample, J152205.41+393441.3 and J164100.10+345452.7, exhibit significant variability across all investigated timescales in the present work (see Table 4), they do not show the systematic wavelength dependence of variability amplitude decrease, namely $\psi_{pp}^g > \psi_{pp}^r > \psi_{pp}^i$ and $F_{\text{var}}^g > F_{\text{var}}^r > F_{\text{var}}^i$ (see Table 2), which would strongly favor a jet-dominated origin. Consequently, the physical drivers of variability in these two RQ-NLSy1s cannot be firmly established based on sub-timescale analysis alone and are therefore further examined through their color-variability behavior, as discussed in the subsequent subsection.

5.2. Color variability

To further discriminate between jet-dominated and accretion disk-dominated emission in the seven RQ-NLSy1s, we place particular emphasis on the color variability results presented in Sect. 4.2. Following the approach adopted in Sect. 4.2, a clear BWB was shown by three sources, J102906.69+555625.2, J123220.11+495721.8 and J150916.18+613716.7 from their diagrams ($g - r$) versus ($g + r$), with Pearson- ρ exceeding 0.5 (see Fig. 4). A similar strong BWB trend is observed for J123220.11+495721.8 and J150916.18+613716.7 in the ($r - i$) versus ($r + i$) diagrams (see Fig. 5). The J102906.69+555625.2

could not be tested in this case due to the lack of data from the *ZTF* *i*-band.

Together with the flux variability results, these color trends strongly indicate that, in three out of the seven RQ-NLSy1s, namely J102906.69+555625.2, J123220.11+495721.8, and J150916.18+613716.7, the optical emission is predominantly driven by jet-related processes. In contrast, the MIR color-magnitude analysis reveals a statistically significant trend only for J150916.18+613716.7, which shows a pronounced RWB behavior in its diagram ($W1 - W2$) versus ($W1 + W2$) (see Fig. 6). This RWB trend suggests an increased contribution from thermal components, such as dust reprocessing and the accretion disk, at MIR wavelengths.

The presence of strong optical BWB trends in these three RQ-NLSy1s, together with a systematic decrease in variability amplitude towards longer wavelengths, that is, $\psi_{\text{pp}}^g > \psi_{\text{pp}}^r > \psi_{\text{pp}}^i$ and $F_{\text{var}}^g > F_{\text{var}}^r > F_{\text{var}}^i$, is consistent with trends reported for BL Lac objects (e.g., see Negi et al. 2022). This behavior supports a scenario in which jet-dominated variability produces correlated flux changes across optical bands, with larger amplitudes at higher frequencies naturally accompanying a BWB spectral evolution.

5.3. Dependence of variability amplitude on AGN parameters

To explore how the long-term optical variability amplitude depends on the physical characteristics of AGNs, we examined the correlations between $\psi_{\text{pp}}^{g, r}$ and several key AGN parameters. The results of these tests are presented in Sect. 4.4. We find a strong anti-correlation between ψ_{pp} and both R_{4570} and R_{5007} , in agreement with earlier studies of NLSy1s (e.g., see Ai et al. 2010; Rakshit & Stalin 2017). This indicates that sources with stronger Fe II and [O III] emission tend to show lower amplitudes of optical variability.

We also detect a significant positive correlation between ψ_{pp} and black hole mass, M_{BH} , consistent with similar trends reported earlier for Quasars (e.g. see Wold et al. 2007; Wilhite et al. 2008). Such a relation can be understood within the framework of accretion disk models in which the mean accretion rate is of the order $\dot{m}_0 \sim 0.1$, with stochastic variations at the level of 0.1–0.5 \dot{m}_0 (Li & Cao 2008). However, Ai et al. (2010) noted that this correlation weakens once the dependence on the Eddington ratio is taken into account.

Nevertheless, we find a strong and fundamental anti-correlation between ψ_{pp} and $\langle R_{\text{Edd}} \rangle$ for our sample of seven RQ-NLSy1s, which is largely independent of the black hole mass (see Ai et al. 2010). This behavior is consistent with previous results for larger samples of NLSy1s (see Rakshit & Stalin 2017; Rakshit et al. 2019). This can be understood within the standard Shakura–Sunyaev accretion disk framework (Shakura & Sunyaev 1973), where the characteristic radius of the disk region emitting at a given wavelength λ scales as $R \propto T^{-4/3} \propto (\dot{m}/M_{\text{BH}})^{1/3} \lambda^{4/3}$, where R is in units of the Schwarzschild radius, T is the temperature of the disk, and \dot{m} is the mass accretion rate in Eddington units. At a fixed wavelength, systems with higher Eddington ratios emit predominantly from larger disk radii, whereas lower Eddington ratio sources are dominated by emission from the inner disk. Since inner disk regions are expected to vary more strongly and on shorter timescales, this naturally leads to an anti-correlation between optical variability amplitude and Eddington ratio.

6. Conclusions

We have presented a comprehensive optical and mid-infrared variability study of seven radio-quiet narrow-line Seyfert 1 galaxies using high-cadence optical data from *ZTF* *g*, *r*, and *i* bands and long-term MIR observations in *WISE* *W1* and *W2* bands. Our main conclusions are summarized below.

1. All seven RQ-NLSy1s exhibit statistically significant long-term optical variability in the *ZTF* *g*, *r*, and *i* bands. The variability amplitudes show a clear wavelength dependence in most cases, with larger amplitudes at shorter wavelengths. In three sources, J102906.69+555625.2, J123220.11+495721.8, and J150916.18+613716.7, both ψ_{pp} and F_{var} decrease systematically from the *g* band to the *i* band, a behavior commonly associated with jet-dominated synchrotron emission.
2. Optical variability on sub-timescales was explored using high-cadence *ZTF* data. Although most sources show weak or absent intra-night and week-like variability in our analysis, the results are broadly consistent with previous INOV studies of the same sample. When considered together, the long-term and short-timescale variability properties support a jet-related origin for optical variability in three RQ-NLSy1s, namely J102906.69+555625.2, J123220.11+495721.8, and J150916.18+613716.7.
3. The mid-infrared variability could be robustly examined for four sources with reliable *WISE* *W1* and *W2* data. Three of these objects, namely J123220.11+495721.8, J150916.18+613716.7, and J164100.10+345452.7, exhibit statistically significant intrinsic MIR variability in both *WISE* *W1* and *W2* bands, suggesting that non-thermal processes contribute to MIR emission, in addition to thermal radiation from the accretion disk and dusty torus.
4. Optical color-magnitude analysis, performed using bias-mitigated $(m_1 - m_2)$ versus $(m_1 + m_2)$ diagrams, reveals a clear bluer-when-brighter trends in three RQ-NLSy1s, namely J102906.69+555625.2, J123220.11+495721.8 and J150916.18+613716.7. These trends are consistent with synchrotron-dominated variability and further strengthen the case for jet-driven optical emission in these sources. In contrast, MIR color variability is detected only in J150916.18+613716.7, which shows a redder-when-brighter trend, likely reflecting an increased contribution from thermal dust emission at longer wavelengths.
5. Cross-correlation analysis using the ICCF method reveals no significant intra-optical inter-band lags, implying nearly simultaneous emission across optical bands. In contrast, significant optical–MIR and MIR intra-band lags are detected in three sources, with MIR emission lags the optical by tens to hundreds of days. These delays are consistent with reprocessing of optical/UV radiation by dust located at parsec-scale distances from the central engine.
6. Based on the broadband SED modeling of six out of seven RQ-NLSy1s, we conclude that these objects host relativistic jets with strong evidence of jet-based emissions from three RQ-NLSy1s, namely J102906.69+555625.2, J123220.11+495721.8, and J150916.18+613716.7.
7. The long-term optical variability amplitude shows strong correlations with the fundamental AGN parameters. In particular, ψ_{pp} anti-correlates with the Eddington ratio and emission-line ratios (R_{4570} and R_{5007}), while positively correlating with black hole mass. These trends are consistent with expectations from standard accretion disk models, where higher Eddington ratio systems emit predominantly from larger, less variable disk radii.

Overall, our results demonstrate that a subset of RQ-NLSy1 galaxies exhibits variability properties remarkably similar to those of jet-dominated AGNs, despite their radio-quiet classification. This suggests that weak or intermittently active jets may play a significant role in shaping the optical and MIR variability of some RQ-NLSy1s. Future coordinated multi-wavelength monitoring, particularly including X-ray and radio observations, will be crucial for establishing the prevalence and physical nature of jet activity in this intriguing class of AGNs.

Acknowledgements. We acknowledge the support of the National Key R&D Program of China (2025YFA1614101) and the National Science Foundation of China (12133001). The work of LCH was supported by the National Science Foundation of China (12233001), the National Key R&D Program of China (2022YFF0503401), and China Manned Space Program (CMS-CSST-2025-A09). H.C. expresses gratitude to the Inter-University Center for Astronomy and Astrophysics (IUCAA), India, for their hospitality under the IUCAA Associate Program. This research utilizes observational data collected with the 48-inch Samuel Oschin Telescope, as part of the Zwicky Transient Facility (ZTF) initiative. The National Science Foundation funds the ZTF project through Grant No. AST-2034437 is a collaborative effort involving institutions such as Caltech, IPAC, the Weizmann Institute of Science, the Oskar Klein Center at Stockholm University, the University of Maryland, DESY and Humboldt University, the TANGO Consortium in Taiwan, the University of Wisconsin–Milwaukee, Trinity College Dublin, Lawrence Livermore National Laboratory, and IN2P3 in France. The operational management of ZTF is handled by Caltech Optical Observatories (COO), IPAC, and the University of Washington. This study also incorporates data from the Wide Field Infrared Survey Explorer (WISE), a collaborative mission between the University of California, Los Angeles, and NASA's Jet Propulsion Laboratory at Caltech, supported by the National Aeronautics and Space Administration.

References

Abdo, A. A., Ackermann, M., Ajello, M., et al. 2009a, *ApJ*, 699, 976
 Abdo, A. A., Ackermann, M., Ajello, M., et al. 2009b, *ApJ*, 707, 727
 Abdo, A. A., Ackermann, M., Ajello, M., et al. 2009c, *ApJ*, 707, L142
 Ai, Y. L., Yuan, W., Zhou, H. Y., et al. 2010, *ApJ*, 716, L31
 Anjum, A., Stalin, C. S., Rakshit, S., Gudennavar, S. B., & Durgapal, A. 2020, *MNRAS*, 494, 764
 Antonucci, R. 1993, *ARA&A*, 31, 473
 Antonucci, R. & Barvainis, R. 1988, *ApJ*, 332, L13
 Bachev, R., Strigachev, A., & Semkov, E. 2005, *MNRAS*, 358, 774
 Bauer, A., Baltay, C., Coppi, P., et al. 2009, *ApJ*, 705, 46
 Bellm, E. C., Kulkarni, S. R., Graham, M. J., et al. 2019, *PASP*, 131, 018002
 Berton, M., Caccianiga, A., Foschini, L., et al. 2017, *Astronomy & Astrophysics*, 605, A48
 Berton, M., Järvelä, E., Crepaldi, L., et al. 2020, *A&A*, 636, A64
 Bicknell, G. V., Dopita, M. A., & O'Dea, C. P. O. 1997, *ApJ*, 485, 112
 Bischetti, M., Piconcelli, E., Vietri, G., et al. 2017, *A&A*, 598, A122
 Brandt, W. N., Mathur, S., & Elvis, M. 1997, *MNRAS*, 285, L25
 Caccianiga, A. et al. 2015, *Astronomy & Astrophysics*, 574, A33
 Cackett, E. M., Horne, K., & Winkler, H. 2007, *MNRAS*, 380, 669
 Chakrabarti, S. K. & Wiita, P. J. 1993, *ApJ*, 411, 602
 Chand, K. & Gopal-Krishna, Hum, C. 2024, *PASA*, 41, e106
 Crepaldi, L., Berton, M., Dalla Barba, B., et al. 2025, *A&A*, 696, A74
 Czerny, B., Siemiginowska, A., Janiuk, A., & Gupta, A. C. 2008, *MNRAS*, 386, 1557
 de Diego, J. A., González-Pérez, J. N., & Kidger, M. R. 1998, *The Astrophysical Journal Supplement Series*, 119, 247
 Dekany, R., Smith, R. M., Riddle, R., et al. 2020, *PASP*, 132, 038001
 Foschini, L. 2011, in *Narrow-Line Seyfert 1 Galaxies and their Place in the Universe*, ed. L. Foschini, M. Colpi, L. Gallo, D. Grupe, S. Komossa, K. Leighly, & S. Mathur, 24
 Foschini, L. 2014, *International Journal of Modern Physics D*, 23, 1430012
 Foschini, L. 2017, *Frontiers in Astronomy and Space Sciences*, 4, 1
 Foschini, L., Berton, M., Caccianiga, A., et al. 2015, *A&A*, 575, A13
 Goodrich, R. W., Stringfellow, G. S., Penrod, G. D., & Filippenko, A. V. 1989, *ApJ*, 342, 908
 Gopal-Krishna, Stalin, C. S., Sagar, R., & Wiita, P. J. 2003, *ApJ*, 586, L25
 Goyal, A., Gopal-Krishna, Wiita, P. J., et al. 2012, *A&A*, 544, A37
 Goyal, A., Gopal-Krishna Paul J., W., Stalin, C. S., & Sagar, R. 2013a, *MNRAS*, 435, 1300
 Goyal, A., Mhaskey, M., Gopal-Krishna, et al. 2013b, *Journal of Astrophysics and Astronomy*, 34, 273
 Grupe, D. & Mathur, S. 2004, *ApJ*, 606, L41
 Gu, M. F. & Ai, Y. L. 2011, *A&A*, 534, A59
 Heckman, T. M. & Best, P. N. 2014, *ARA&A*, 52, 589
 Heidt, J. & Wagner, S. J. 1996, *A&A*, 305, 42
 Heinz, S. & Sunyaev, R. A. 2003, *MNRAS*, 343, L59
 Ikejiri, Y., Uemura, M., Sasada, M., et al. 2011, *PASJ*, 63, 639
 Jang, M. & Miller, H. R. 1995, *ApJ*, 452, 582
 Jarrett, T. H., Cohen, M., Masci, F., et al. 2011, *ApJ*, 735, 112
 Jarvela, E., Lähteenmäki, A., Lietzen, H., et al. 2017, *A&A*, 606, A9
 Jarvela, E., Savolainen, T., Berton, M., et al. 2024, *MNRAS*, 532, 3069
 Kawaguchi, T., Mineshige, S., Umemura, M., & Turner, E. L. 1998, *The Astrophysical Journal*, 504, 671
 Kellermann, K. I., Sramek, R., Schmidt, M., Shaffer, D. B., & Green, R. 1989, *AJ*, 98, 1195
 Kirk, J. G., Rieger, F. M., & Mastichiadis, A. 1998, *A&A*, 333, 452
 Komossa, S. 2018, in *Revisiting Narrow-Line Seyfert 1 Galaxies and their Place in the Universe*, 15
 Koshida, S., Minezaki, T., Yoshii, Y., et al. 2014, *ApJ*, 788, 159
 Lähteenmäki, A., Järvelä, E., Ramakrishnan, V., et al. 2018, *A&A*, 614, L1
 Larionov, V. M., Villata, M., & Raiteri, C. M. 2010, *A&A*, 510, A93
 Lawrence, A. 2018, *Nature Astronomy*, 2, 102
 Li, S.-L. & Cao, X. 2008, *MNRAS*, 387, L41
 Liska, M., Chatterjee, K., Tchekhovskoy, A., et al. 2022, *The Astrophysical Journal Supplement Series*, 258, 31
 Lu, W., Kumar, P., & Evans, N. J. 2016, *MNRAS*, 458, 575
 Lynden-Bell, D. 1969, *Nature*, 223, 690
 MacLeod, C. L., Ivezic, Z., Kochanek, C. S., et al. 2010, *ApJ*, 721, 1014
 Mandal, A. K., Rakshit, S., Kurian, K. S., et al. 2018, *MNRAS*, 475, 5330
 Mangalam, A. V. & Wiita, P. J. 1993, *ApJ*, 406, 420
 Marscher, A. P. 2014, *ApJ*, 780, 87
 Marscher, A. P. & Gear, W. K. 1985, *ApJ*, 298, 114
 Marscher, A. P., Jorstad, S. G., D'Arcangelo, F. D., et al. 2008, *Nature*, 452, 966
 Masci, F. J., Laher, R. R., Rusholme, B., et al. 2019, *PASP*, 131, 018003
 Mastichiadis, A. & Kirk, J. G. 2002, *PASA*, 19, 138
 Mathur, S. 2000, *MNRAS*, 314, L17
 McHardy, I. M., Cameron, D. T., Dwelly, T., et al. 2014, *MNRAS*, 444, 1469
 McKinney, J. C., Tchekhovskoy, A., & Blandford, R. D. 2017, *Monthly Notices of the Royal Astronomical Society*, 467, 4393
 Monet, D. G. 1998, in *Bulletin of the American Astronomical Society*, Vol. 30, American Astronomical Society Meeting Abstracts, 1427
 Negi, V., Gopal-Krishna, Joshi, R., et al. 2023, *MNRAS*, 522, 5588
 Negi, V., Joshi, R., Chand, K., et al. 2022, *MNRAS*, 510, 1791
 Noda, H. & Done, C. 2018, *Monthly Notices of the Royal Astronomical Society*, 480, 3898
 Ojha, V. 2022, *Journal of Astrophysics and Astronomy*, 43, 25
 Ojha, V., Hum, C., Dewangan, G. C., & Rakshit, S. 2020, *ApJ*, 896, 95
 Ojha, V., Hum, C., & Gopal-Krishna. 2018, *Bulletin de la Societe Royale des Sciences de Liege*, 87, 387
 Ojha, V., Jha, V. K., Chand, H., & Singh, V. 2022, *MNRAS*, 514, 5607
 Ojha, V., Singh, V., Berton, M., & Järvelä, E. 2024, *MNRAS*, 529, L108
 Ojha, V., Wu, X.-B., & Ho, L. C. 2025, *ApJ*, 994, 84
 Osterbrock, D. E. & Pogge, R. W. 1985, *ApJ*, 297, 166
 Padovani, P. 2017, *Frontiers in Astronomy and Space Sciences*, 4, 35
 Paliya, V. S. 2019, *Journal of Astrophysics and Astronomy*, 40, 39
 Paliya, V. S., Stalin, C. S., Kumar, B., et al. 2013, *MNRAS*, 428, 2450
 Papadakis, I. E., Villata, M., & Raiteri, C. M. 2007, *A&A*, 470, 857
 Peterson, B. M., Ferrarese, L., Gilbert, K. M., et al. 2004, *ApJ*, 613, 682
 Rakshit, S., Johnson, A., Stalin, C. S., Gandhi, P., & Hoenig, S. 2019, *MNRAS*, 483, 2362
 Rakshit, S. & Stalin, C. S. 2017, *ApJ*, 842, 96
 Rees, M. J. 1984, *ARA&A*, 22, 471
 Romero, G. E., Cellone, S. A., & Combi, J. A. 1999, *A&AS*, 135, 477
 Sagar, R., Stalin, C. S., Gopal-Krishna, & Wiita, P. J. 2004, *MNRAS*, 348, 176
 Schlafly, E. F. & Finkbeiner, D. P. 2011, *ApJ*, 737, 103
 Sesar, B., Ivezic, Z., Lupton, R. H., et al. 2007, *AJ*, 134, 2236
 Shakura, N. I. & Sunyaev, R. A. 1973, *A&A*, 24, 337
 Singh, V., Kumar, P., Das, A. K., & Ojha, V. 2025, *ApJ*, 990, 79
 Stalin, C. S., Gopal-Krishna, Sagar, R., & Wiita, P. J. 2004, *Journal of Astrophysics and Astronomy*, 25, 1
 Stalin, C. S. & Srianand, R. 2005, *MNRAS*, 359, 1022
 Storchi-Bergmann, T., Mulchaey, J. S., & Wilson, A. S. 1992, *ApJ*, 395, L73
 Suganuma, M., Yoshii, Y., Kobayashi, Y., et al. 2006, *ApJ*, 639, 46
 Türler, M. 2011, *Mem. Soc. Astron. Italiana*, 82, 104
 Ulrich, M.-H., Maraschi, L., & Urry, C. M. 1997, *ARA&A*, 35, 445
 Urry, C. M. & Padovani, P. 1995, *PASP*, 107, 803
 Vagnetti, F., Trevese, D., & Neseli, R. 2003, *ApJ*, 590, 123
 Vaughan, S., Edelson, R., Warwick, R. S., & Uttley, P. 2003, *MNRAS*, 345, 1271
 Véron-Cetty, M.-P., Véron, P., & Gonçalves, A. C. 2001, *A&A*, 372, 730
 Villata, M., Raiteri, C. M., Kurtanidze, O. M., et al. 2004, *A&A*, 421, 103
 Villata, M., Raiteri, C. M., Kurtanidze, O. M., et al. 2002, *A&A*, 390, 407
 Wagner, S. J. & Witzel, A. 1995, *ARA&A*, 33, 163
 Wang, H.-T. & Shi, Y. 2020, *Research in Astronomy and Astrophysics*, 20, 021
 Wiita, P. J., Miller, H. R., Carini, M. T., & Rosen, A. 1991, in *IAU Colloq. 129: The 6th Institute d'Astrophysique de Paris (IAP) Meeting: Structure and Emission Properties of Accretion Disks*, ed. C. Bertout, S. Collin-Souffrin, & J. P. Lasota, 557
 Wilhite, B. C., Brunner, R. J., Grier, C. J., Schneider, D. P., & vanden Berk, D. E. 2008, *MNRAS*, 383, 1232
 Wold, M., Brotherton, M. S., & Shang, Z. 2007, *MNRAS*, 375, 989
 Woo, J.-H. & Urry, C. M. 2002, *ApJ*, 579, 530
 Wright, E. L., Eisenhardt, P. R. M., Mainzer, A. K., et al. 2010, *AJ*, 140, 1868
 Zhou, H., Wang, T., Yuan, W., et al. 2006, *ApJS*, 166, 128

Appendix A: Light curves and lag measurements

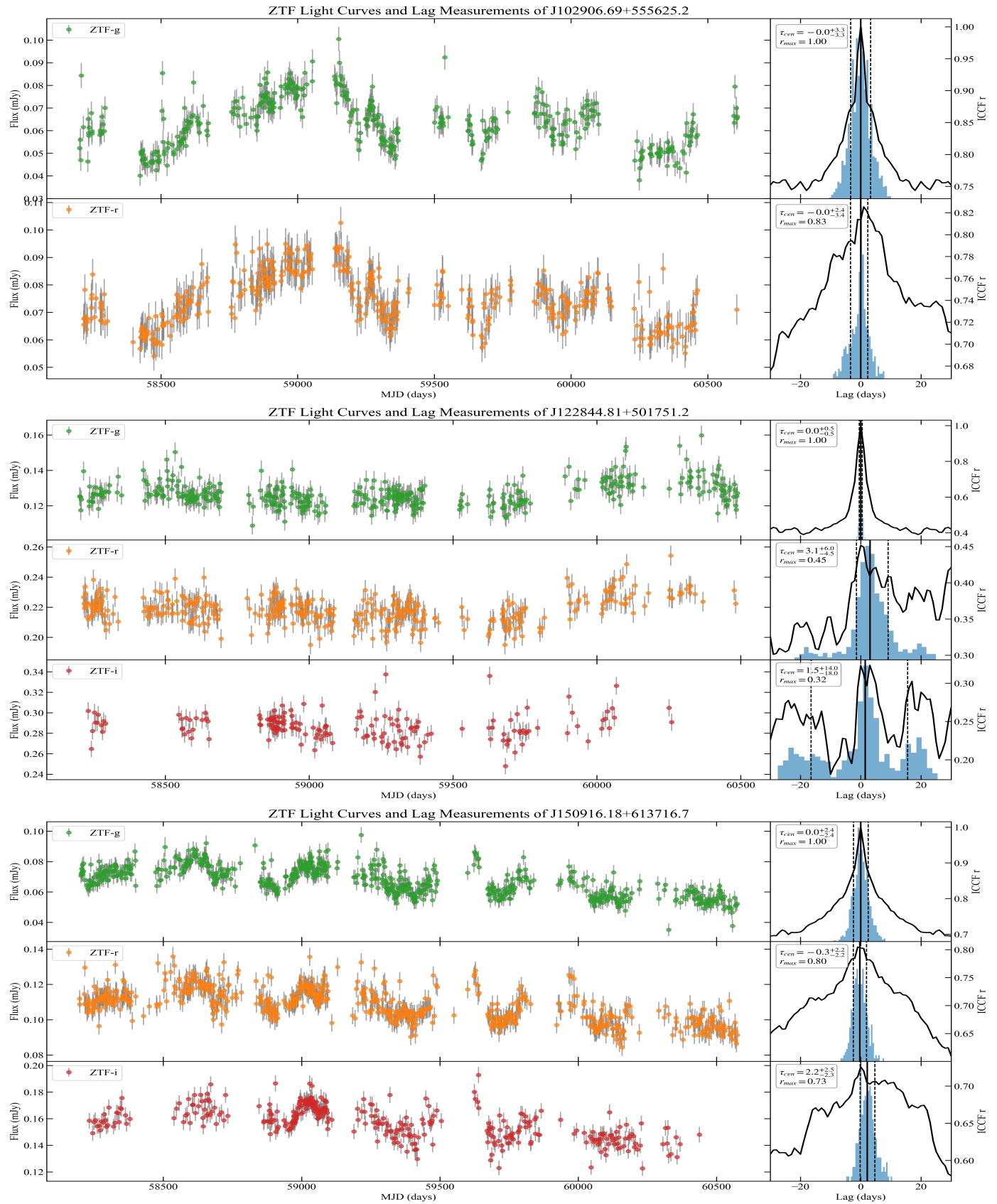


Fig. A.1: same as Fig. 7 but for the source J102906.69+555625.2, J122844.81+501751.2, and J151020.06+554722.0.

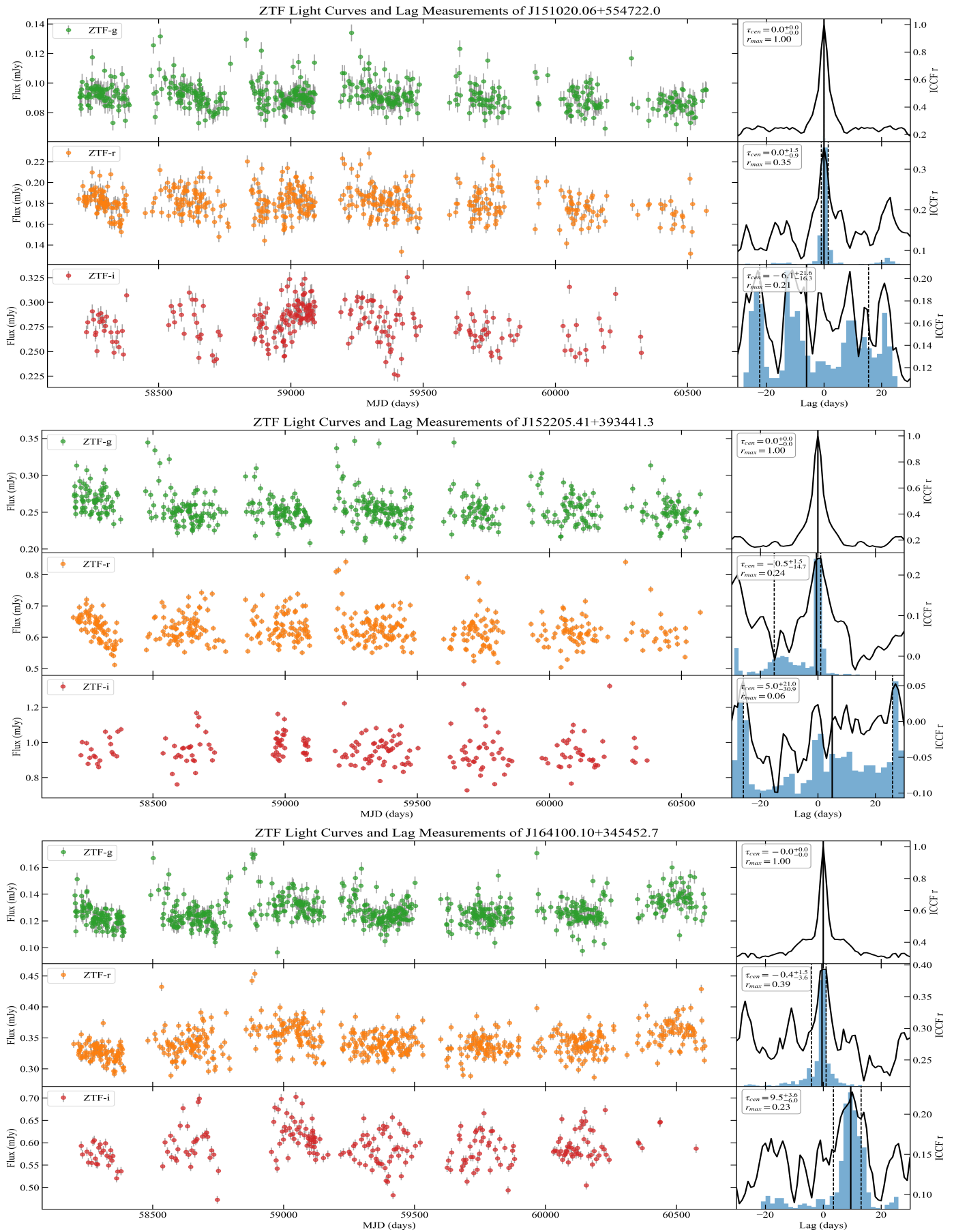


Fig. A.2: same as Fig. 7 but for the sources J151020.06+554722.0, J152205.41+393441.3, and J164100.10+345452.7.

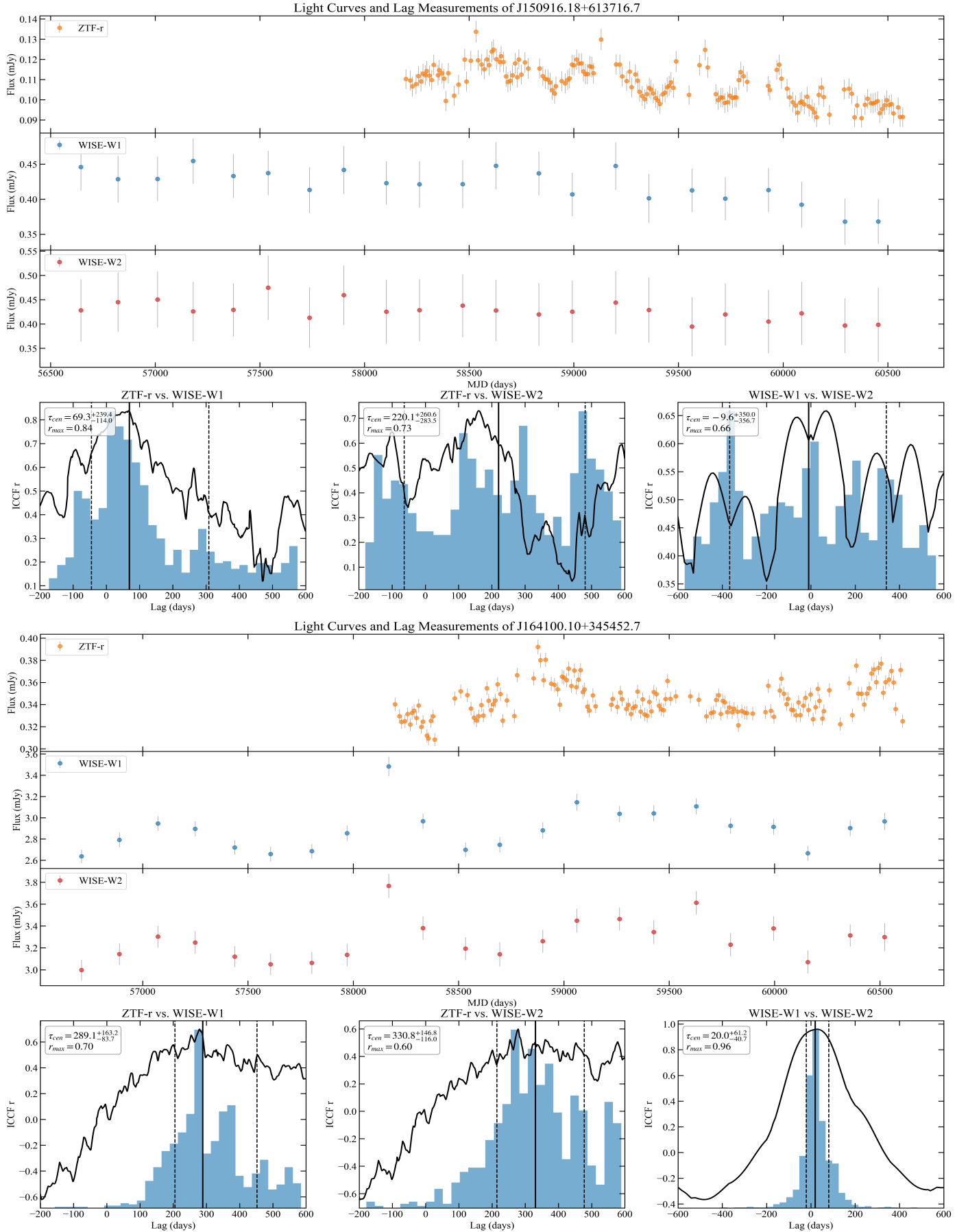


Fig. A.3: Same as Fig. 8 but for the sources J150916.18+613716.7 and J164100.10+345452.7.